Key Points:
- FORC simulations performed for strongly interacting SD particles
- FORC signatures found for clusters and chains
- Presence and degree of bacterial chain collapse quantified

Supporting Information:
- Readme
- Supplemental Figures
- FORCulator
- FORCulator Quick Start Guide

Correspondence to:
R. J. Harrison,
rjh40@esc.cam.ac.uk

FORCulator: A micromagnetic tool for simulating first-order reversal curve diagrams

Richard J. Harrison[1] and Ioan Lascu[1]

[1]Department of Earth Sciences, University of Cambridge, Cambridge, UK

Abstract We describe a method for simulating first-order reversal curve (FORC) diagrams of interacting single-domain particles. Magnetostatic interactions are calculated in real space, allowing simulations to be performed for particle ensembles with arbitrary geometry. For weakly interacting uniaxial particles, the equilibrium magnetization at each field step is obtained by direct solution of the Stoner-Wohlfarth model, assuming a quasi-static distribution of interaction fields. For all other cases, the equilibrium magnetization is calculated using an approximate iterated solution to the Landau-Lifshitz-Gilbert equation. Multithreading is employed to allow multiple curves to be computed simultaneously, enabling FORC diagrams to be simulated in reasonable time using a standard desktop computer. Statistical averaging and post processing lead to simulated FORC diagrams that are comparable to their experimental counterparts. The method is applied to several geometries of relevance to rock and environmental magnetism, including densely packed random clusters and partially collapsed chains. The method forms the basis of *FORCulator*, a freely available software tool with graphical user interface that will enable FORC simulations to become a routine part of rock magnetic studies.

1. Introduction

First-order reversal curve (FORC) diagrams are an advanced hysteresis measurement that has become a standard characterization tool in rock magnetism [*Pike et al.*, 1999; *Roberts et al.*, 2000, 2014; *Harrison et al.*, 2007]. From a magnetic perspective, typical rocks can be described as multicomponent ensembles of magnetic particles with varying shapes, sizes, domain states, coercivities, and spatial distributions. This complexity means that traditional analysis of bulk hysteresis parameters [*Dunlop*, 2002a, 2002b] can often lead to an ambiguous or misleading assessment of a rock's magnetic mineralogy. FORC diagrams, on the other hand, offer the possibility of unambiguous domain-state fingerprinting, extraction of domain-state-specific coercivity distributions, the detection of geometry-specific magnetostatic interaction fields, and a quantitative analysis of magnetic mixtures [*Ludwig et al.*, 2013; *Roberts et al.*, 2014]. Recent applications of FORC diagrams include the detection of biogenic magnetite signals in sediments [*Egli et al.*, 2010], determining the nucleation and annihilation fields for single-vortex states in dusty olivine [*Lappe et al.*, 2011], prescreening of samples prior to paleointensity measurements [*Carvallo et al.*, 2006], quantitative modeling of remanence acquisition [*Muxworthy and Heslop*, 2011; *Muxworthy et al.*, 2011; *Lappe et al.*, 2013], and the unmixing of central-ridge signatures for environmental magnetic applications [*Egli et al.*, 2010; *Egli*, 2013; *Ludwig et al.*, 2013; *Roberts et al.*, 2013; *Heslop et al.*, 2014].

A long-term goal of FORC research is to create an inverse method to transform an observed FORC diagram into a realistic physical model of the underlying magnetic ensemble. Before inverse methods can be developed, however, it is necessary to have a comprehensive understanding of the forward problem. There have been some significant steps toward this goal for weakly interacting particles [*Egli*, 2006], but there is a gap in our understanding of FORC diagrams for strongly interacting particles, which are commonplace in natural systems, e.g., in intergrowths [*Harrison et al.*, 2002; *Evans et al.*, 2006; *Feinberg et al.*, 2006], magnetotactic bacteria [*Chen et al.*, 2007; *Li et al.*, 2012, 2013], clay-magnetite aggregates [*Galindo-Gonzalez et al.*, 2009], and framboids [*Kimura et al.*, 2013]. The aim of this paper is to develop a tool that solves the forward problem of generating FORC diagrams for strongly interacting single-domain particles with arbitrary spatial arrangement. The method forms the basis of *FORCulator*, a freely available software tool with graphical user interface that will enable FORC simulations to become a routine part of rock magnetic studies. The method is applied to several test cases of relevance to rock magnetism, illustrating how strong magnetostatic

interactions between particles lead to geometry-specific signatures in FORC diagrams that inform our understanding of the underlying magnetic mineralogy.

2. FORC Simulation Approaches: Pros and Cons

Several methods for simulating FORC diagrams have been successfully employed in the past. Here we review the advantages and disadvantages of each method within the context of the aims of this study, before justifying our chosen approach.

2.1. Preisach Modeling

Much of the pioneering work on simulating FORC diagrams has been done within the framework of Preisach theory [*Pike et al.*, 1999]. In Preisach theory [*Preisach*, 1935], each particle is described by a hysteron with a specified coercivity, B_c, and horizontal offset, B_u. The horizontal offset is the result of a static local interaction field, $B^{int} = -B_u$, and the FORC distribution (ρ) is the product of independent coercivity and interaction-field distributions $\rho(B_c, B_u) = f(B_c)g(B_u)$. Various modifications to the standard Preisach model have been developed to deal with strongly interacting systems. In the "moving" Preisach model [*Stancu et al.*, 2001], a mean-field interaction shifts the peak in $g(B_u)$ by an amount proportional to the net magnetic moment of the ensemble. A positive or negative shift accounts for the collective magnetizing or demagnetizing effects of specific geometries [*Pike et al.*, 1999; *Stancu et al.*, 2003]. Further adaptations, such as the "variable variance" Preisach model adjust both the shift and the width of $g(B_u)$ as a function of net moment, or even allow for a double peaked distribution of interaction fields for very strongly interacting systems [*Stancu et al.*, 2004]. These modified Preisach models provide a quick and flexible framework for simulating FORC diagrams that compare well with their experimental counterparts. However, this approach is phenomenological in nature: it relies on an assumption of how the statistical properties of the interaction-field distribution evolve with the magnetic state of the ensemble. They are not, therefore, suited to the prediction of FORC diagrams for arbitrary geometries.

2.2. Analytical Solutions

An analytical solution for noninteracting Stoner-Wohlfarth particles was presented by *Newell* [2005]. This work explained several key features of FORC diagrams, such as the infinitely sharp "central-ridge" signal along the $B_u = 0$ axis, the combination of positive and negative background signals for $B_u < 0$, and the absence of signal for $B_u > 0$. A model of weakly interacting particles was presented by *Egli* [2006], which provides an analytical expression for the broadening of the central-ridge signal. The main advantages of an analytical approach are speed, accuracy, and the ability to extract quantitative information about the sample (e.g., particle packing fractions) via curve fitting [*Chen et al.*, 2007]. The main disadvantage is the lack of generality: analytical solutions must be created on a case by case basis, so this approach is not suited to the prediction of FORC diagrams for arbitrary geometries. Furthermore, current solutions are restricted to uniformly magnetized single-domain (SD) particles and to the noninteracting and weakly interacting cases.

2.3. Micromagnetic Modeling

Micromagnetic modeling represents the state of the art for computing the magnetic response of a system [*Fidler and Schrefl*, 2000], and has played a central role in developing our understanding of the relationship between magnetostatic interactions and FORC diagrams [*Muxworthy and Williams*, 2005]. Using micromagnetic simulations, it is possible to calculate FORC diagrams for strongly interacting systems (including the effects of both magnetostatic and exchange interactions) [*Muxworthy et al.*, 2004], account for pseudo-single-domain (PSD) and multidomain (MD) states [*Carvallo et al.*, 2003], and deal with heterogeneous systems [*Schrefl et al.*, 2012]. The main disadvantage of micromagnetic modeling is that calculations are relatively slow and resource intensive. They are typically performed by experts in computer simulation who have access to considerable computing resources—they are not suited to routine application by nonspecialists using a standard desktop computer. The computational overhead means that micromagnetic simulations are often restricted in the number of particles that can be included and/or the number of times different statistical distributions of particles can be sampled to generate a smoothed FORC diagram. For this reason, FORC diagrams calculated via micromagnetic modeling are often too noisy to allow useful comparison with their experimental counterparts [*Carvallo et al.*, 2003].

2.4. Simplified Micromagnetic Modeling

For systems dominated by SD particles, a simplified micromagnetic approach, based on interacting ensembles of Stoner-Wohlfarth particles, becomes a good physical approximation [*Stancu et al.*, 2003]. Each

particle sees an effective magnetic field, which is the sum of the applied field, an anisotropy field, and a magnetostatic interaction field. The equilibrium magnetization of the ensemble is calculated by numerical integration of the Landau-Lifshitz-Gilbert (LLG) equation, taking full account of dipole-dipole magnetostatic interactions at each step. For specific geometries, the simplified micromagnetic approach has been shown to yield identical results to the modified Preisach model [*Stancu et al.*, 2003]. However, the simplified micromagnetic approach has a far greater predictive power. Calculations can be performed for arbitrary geometries, and since the computational overhead is significantly less than for full micromagnetic simulations, they can be performed for larger systems and/or multiple times to generate better statistical averaging. Like full micromagnetic simulations, the simplified micromagnetic approach is suitable for strongly interacting and highly correlated systems. The key disadvantages of the method are that it is not (currently) amenable to routine application by nonspecialists in computer simulations, it is slow in comparison to analytical or Preisach approaches, and it is restricted to SD particles.

2.5. Our Approach

Given the aims of this study, we have adopted a method based on the simplified micromagnetic approach of *Stancu et al.* [2003], with specific improvements aimed at (a) speeding up the calculation of FORCs, (b) extending from the regular 2-D geometry of *Stancu et al.* [2003] to an arbitrary 3-D geometry, (c) extending the method to include particles with cubic as well as uniaxial anisotropy, and (d) creating a graphical user interface that is amenable to routine application by nonspecialists in computer simulations. Our motivation is to facilitate the routine simulation of FORC diagrams in rock magnetic studies, with applications both to research and teaching.

3. Methods

3.1. Theory

The magnetic ensemble consists of N uniformly magnetized SD particles arranged arbitrarily inside a 3-D space. The position of the ith particle is specified by the coordinates $\boldsymbol{R}_i = (X_i, Y_i, Z_i)$ and its magnetic moment is $\boldsymbol{M}_i = M_{si}V_i \boldsymbol{m}_i$, where M_{si} is saturation magnetization, V_i is volume, and $\boldsymbol{m}_i = (m_i^x, m_i^y, m_i^z)$ is a unit vector. The magnetic state of the ith particle is determined by the total effective field, $\boldsymbol{B}_i^{\text{eff}}$, acting upon it:

$$B_i^{eff} = B^{app} + B_i^{ani} + B_i^{int} \tag{1}$$

$\boldsymbol{B}^{app}$ is the applied magnetic field (acting on all particles), $\boldsymbol{B}_i^{ani}$ is the anisotropy field acting on the ith particle, and $\boldsymbol{B}_i^{int}$ is the magnetostatic interaction field acting on the ith particle. Anisotropy is either uniaxial or cubic. The easy axis of a particle with uniaxial anisotropy is defined by the unit vector $\boldsymbol{u}_i = (u_i^x, u_i^y, u_i^z)$. For uniaxial particles, the anisotropy field is:

$$B_i^{ani} = \frac{2K_{ui}}{M_{si}} m_{i,u} \boldsymbol{u}_i \tag{2}$$

where K_{ui} is the uniaxial anisotropy constant and $m_{i,u}$ is the component of $\boldsymbol{m}_i$ along $\boldsymbol{u}_i$. For convenience, the uniaxial anisotropy of each particle is specified using the parameter $B_{Ki} = 2K_{ui}/M_{si}$, which corresponds to the intrinsic switching field of the particle (in Tesla). The three reference axes of a particle with cubic anisotropy are specified by three orthogonal unit vectors $\boldsymbol{c}_{ij} = (c_{ij}^x, c_{ij}^y, c_{ij}^z)$, where $j = 1, 2, 3$. The effective anisotropy field in this case is:

$$B_i^{ani} = \frac{2K_{ci}}{M_{si}} \left[m_{i,1}\left(m_{i,2}^2 + m_{i,3}^2\right)\boldsymbol{c}_{i1} + m_{i,2}\left(m_{i,3}^2 + m_{i,1}^2\right)\boldsymbol{c}_{i2} + m_{i,3}\left(m_{i,1}^2 + m_{i,2}^2\right)\boldsymbol{c}_{i3} \right] \tag{3}$$

where K_{ci} is the cubic anisotropy constant, and $m_{i,j}$ is the component of $\boldsymbol{m}_i$ along the $\boldsymbol{c}_{ij}$ axis. Again, for convenience, the anisotropy of each particle is specified using the parameter $B_{Ki} = 2K_{ci}/M_{si}$.

The magnetostatic interaction field acting on the ith particle is the sum of the dipolar stray fields created by all other particles in the ensemble. The interaction fields are calculated assuming point dipoles using a matrix of Green's functions [*Weiss et al.*, 2007]:

$$B^{int} = JM \tag{4}$$

where:

$$\boldsymbol{B}^{int} = \begin{bmatrix} B_1^x & B_1^y & B_1^z & B_2^x & B_2^y & B_2^z & \dots & B_N^z \end{bmatrix}^T \tag{5}$$

$$\boldsymbol{M} = \begin{bmatrix} M_1^x & M_1^y & M_1^z & M_2^x & M_2^y & M_2^z & \dots & M_N^z \end{bmatrix}^T \tag{6}$$

$$\boldsymbol{J} = \begin{bmatrix} \partial B_1^x/\partial M_1^x & \partial B_1^x/\partial M_1^y & \partial B_1^x/\partial M_1^z & \partial B_1^x/\partial M_2^x & \partial B_1^x/\partial M_2^y & \partial B_1^x/\partial M_2^z & \dots & \partial B_1^x/\partial M_N^z \\ \partial B_1^y/\partial M_1^x & \partial B_1^y/\partial M_1^y & \partial B_1^y/\partial M_1^z & \partial B_1^y/\partial M_2^x & \partial B_1^y/\partial M_2^y & \partial B_1^y/\partial M_2^z & \dots & \partial B_1^y/\partial M_N^z \\ \partial B_1^z/\partial M_1^x & \partial B_1^z/\partial M_1^y & \partial B_1^z/\partial M_1^z & \partial B_1^z/\partial M_2^x & \partial B_1^z/\partial M_2^y & \partial B_1^z/\partial M_2^z & \dots & \partial B_1^z/\partial M_N^z \\ . & . & . & . & . & . & . & . \\ . & . & . & . & . & . & . & . \\ . & . & . & . & . & . & . & . \\ \partial B_N^z/\partial M_1^x & \partial B_N^z/\partial M_1^y & \partial B_N^z/\partial M_1^z & \partial B_N^z/\partial M_2^x & \partial B_N^z/\partial M_2^y & \partial B_N^z/\partial M_2^z & \dots & \partial B_N^z/\partial M_N^z \end{bmatrix} \tag{7}$$

with:

$$\partial B_i^x/\partial M_j^x = 3\mu_0 x_{ij}^2/4\pi r_{ij}^5 - \mu_0/4\pi r_{ij}^3$$

$$\partial B_i^x/\partial M_j^y = 3\mu_0 x_{ij} y_{ij}/4\pi r_{ij}^5$$

$$\partial B_i^x/\partial M_j^z = 3\mu_0 x_{ij} z_{ij}/4\pi r_{ij}^5$$

$$\partial B_i^y/\partial M_j^x = 3\mu_0 y_{ij} x_{ij}/4\pi r_{ij}^5$$

$$\partial B_i^y/\partial M_j^y = 3\mu_0 y_{ij}^2/4\pi r_{ij}^5 - \mu_0/4\pi r_{ij}^3 \tag{8}$$

$$\partial B_i^y/\partial M_j^z = 3\mu_0 y_{ij} z_{ij}/4\pi r_{ij}^5$$

$$\partial B_i^z/\partial M_j^x = 3\mu_0 z_{ij} x_{ij}/4\pi r_{ij}^5$$

$$\partial B_i^z/\partial M_j^y = 3\mu_0 z_{ij} y_{ij}/4\pi r_{ij}^5$$

$$\partial B_i^z/\partial M_j^z = 3\mu_0 z_{ij}^2/4\pi r_{ij}^5 - \mu_0/4\pi r_{ij}^3$$

where $x_{ij} = x_i - x_j$, $y_{ij} = y_i - y_j$, $z_{ij} = z_i - z_j$, $r_{ij} = (x_{ij}^2 + y_{ij}^2 + z_{ij}^2)^{0.5}$, and μ_0 is the permeability of free space.

The dynamic response of a particle to the effective field is governed by the Landau-Lifshitz-Gilbert (LLG) equation:

$$\frac{d\boldsymbol{m}_i}{dt} = -\frac{\gamma}{1+\alpha^2} \boldsymbol{m}_i \times \boldsymbol{B}_i^{eff} - \frac{\gamma\alpha}{(1+\alpha^2)M_{si}} \boldsymbol{m}_i \times \left(\boldsymbol{m}_i \times \boldsymbol{B}_i^{eff}\right) \tag{9}$$

where γ is the gyromagnetic frequency and α is a damping parameter. The LLG equation describes a damped precessional motion of the magnetic moment around the effective field, with equilibrium being achieved when $d\boldsymbol{m}_i/dt = 0$, i.e., when $\boldsymbol{m}_i$ is parallel to $\boldsymbol{B}_i^{eff}$. Direct integration of the LLG equation in the time domain was explored (and remains an option in *FORCulator*), but slow convergence was found to limit the practicality of this method for FORC simulations. Instead, we adopt an approximate method, whereby the magnetic configuration is relaxed iteratively by placing each magnetization vector close to the effective field vector throughout the ensemble. The moment orientation during iteration $n + 1$ is given by $\boldsymbol{m}_i(n + 1) = (1 - f)\, \boldsymbol{m}_i(n) + f\, \boldsymbol{b}_i^{eff}$, where $\boldsymbol{b}_i^{eff}$ is a unit vector parallel to the effective field and f is a damping factor ($0 < f < 1$). This method is equivalent to minimizing the free energy of the system. Higher values of f lead to more rapid convergence. If f is set too high, however, it can lead to oscillatory behavior. A value of $f \sim 0.9$ was used in all the simulations presented here, which provided the best compromise between the desire to minimize convergence time and the need to avoid oscillation. This method works best for uniaxial systems and cubic systems with negative K_c (i.e., <111> easy axes), where the anisotropy field is parallel to the easy axes. The method is less efficient for cubic systems with positive K_c (i.e., <100> easy axes), where the anisotropy field is defined as being antiparallel to the hard axes rather than being parallel to the easy axes. In this case, when other contributions to the effective field are small, placing the moments close to the effective field does not produce the desired effect, and can lead to oscillatory behavior with large f. This can be avoided by using a small value of f (e.g., 0.05–0.1) at the cost of reducing the efficiency of the method. In this paper we consider only uniaxial and cubic systems with $K_c < 0$, which are the most relevant cases for rock magnetism ($K_c < 0$ for magnetite at room temperature).

Simulations are iterated until convergence is reached. We define convergence to have been achieved when the mean magnitude of the torque, τ, is below a certain value, i.e., when:

$$\tau = \frac{1}{N} \sum_{t=1}^{N} |\boldsymbol{m_i} \times \boldsymbol{b_i^{eff}}| < C_{lim} \tag{10}$$

A value of $C_{lim} = 10^{-4}$ was used throughout this paper, which provided adequate equilibration of the net moment in a reasonable time. A maximum number of iterations per field step can be defined, after which the field step is incremented regardless of whether convergence was achieved or not. This number is set large enough to allow virtually all field steps to converge, but small enough to prevent the entire simulation from stalling in case one particular field step takes an unreasonable time to converge. A limit of 500 iterations per field step was used throughout this paper.

An alternative simulation method for uniaxial particles is also made available in *FORCulator*, based on numerical solution of the Stoner-Wohlfarth model in either a static or a quasi-static interaction field [*Newell*, 2005]. In the Stoner-Wohlfarth model, the micromagnetic energy of the *i*th particle is given by:

$$E_i = K_{ui} V_i \sin^2(\theta_i) - B_i M_{si} V_i \cos(\phi_i - \theta_i) \tag{11}$$

where θ_i is the angle between the easy axis and the magnetic moment of the *i*th particle, and φ_i is the angle between the easy axis and magnetic field, B_i, acting on the *i*th particle. B_i is the sum of both the external applied field and the interaction field. Dividing equation (11) by $M_{si} V_i B_{Ki}$, the energy is obtained in reduced units:

$$\eta_i = \frac{1}{2} \sin^2(\theta_i) - b_i \cos(\phi_i - \theta_i) \tag{12}$$

where $b_i = B_i/B_{Ki}$. Stable solutions are defined by:

$$\frac{d\eta_i}{d\theta_i} = \frac{1}{2} \sin(2\theta_i) - b_i \sin(\phi_i - \theta_i) = 0 \tag{13}$$

$$\frac{d^2\eta_i}{d\theta_i^2} = \cos(2\theta_i) + b_i \cos(\phi_i - \theta_i) > 0 \tag{14}$$

Equations (13) and (14) are solved numerically to obtain the equilibrium magnetization state of a given particle. In general, there are two solutions, representing the upper and lower branches of the hysteresis loop. The choice of solution depends on the history of magnetic fields applied to the particle. The switching history of each particle is tracked throughout the simulation and used to determine the correct solution in each case. For the purposes of solving equations (13) and (14), the interaction field can be treated as static, in which case, the stray field is calculated once per ensemble and held constant throughout the calculation. This is equivalent to the standard Preisach approach. Alternatively, it can be treated as quasi static, in which case, the stray field is calculated at the end of the previous field step (via equation (4)) and held constant while the new moment configuration is calculated. The stray field is then updated to reflect the new moment orientations before the calculation proceeds to the next field step. In the static case, the user must specify what configuration of moments should be used to calculate the stray field (e.g., saturated or random moments). In the quasi-static case, the moment configuration is inherited from the previous field step, enabling the interaction-field distribution to evolve throughout the simulation in response to the changes in the overall magnetization state of the ensemble. In this sense, it is similar to the moving Preisach models discussed in section 2.1, and for the case of weakly interacting particles, provides solutions that are similar to the robust statistical approach of *Egli* [2006]. This method is much faster than those based on iterative solution of the LLG equation. However, the approach is restricted to weakly interacting systems, where the assumption of a quasi-static interaction field is valid.

3.2. FORC Simulation

The FORC protocol is well documented in the rock magnetism literature. Readers unfamiliar with the method are referred to *Roberts et al.* [2014] for a detailed review. To initiate a FORC simulation, the user first specifies the basic physical properties of the ensemble, including the number, volume and saturation magnetization of the particles. Second, the user defines the statistical properties of the ensemble, including the

type of spatial arrangement (e.g., random packing versus chains), numerical parameters defining the spatial arrangement (e.g., dimensions of the cubic box into which particles are placed, packing fraction for random packing, number of particles and distance between particles for chains), the type and orientation of anisotropy axes (e.g., uniaxial versus cubic, random versus aligned) and the switching field distribution from which the individual B_{Ki} values will be chosen (e.g., lognormal or user-specified distribution). The goal is to specify the ensemble in a generic way, so that ensembles with similar characteristics can be generated automatically, and their resulting FORC diagrams averaged to provide the final result. Third, the user specifies the type of simulation to be run (e.g., approximate or time-integrated LLG, static or quasi-static Stoner-Wohlfarth) and the simulation parameters (e.g., f factor for approximate LLG, α and γ factors for time-integrated LLG, maximum number of iterations and the convergence limit). Finally, the user defines the desired upper limits of coercivity (B_c) and interaction field (B_u) for the final FORC diagram, together with the desired number of FORC curves (N_{FORC}), the field step size (ΔB), and the number of times the simulation is to be repeated for averaging (N_{avg}).

The ensemble is initialized in a fully saturated state. The simulation begins with a calculation of the upper branch of the hysteresis loop, starting at a field of ($B_u + N_{FORC}\Delta B$) and finishing at a field of ($B_u - [N_{FORC} - 1]\Delta B$) in steps of ΔB. The simulation is converged at each field step, with the configuration of moments obtained at the end of each field step serving as the starting configuration for the next. The configuration of moments obtained at each applied field, B_r, between B_u and ($B_u - [N_{FORC} - 1]\Delta B$) corresponds to the starting configuration for each of the required FORCs. Individual FORC curves are simulated independently as the field (B) increases from B_r to ($B - B_r$)/2 $\leq B_c$ in steps of ΔB. Automatic multithreading is employed to take advantage of multiple processors, if available. The simulations described here were performed using an Apple iMac with a 3.4 GHz Intel Quad Core i7 processor and 16 GB RAM, which enabled eight FORCs to be calculated simultaneously. After simulating N_{FORC} curves for the given ensemble, a new ensemble is generated based on the specified characteristics. This process is repeated N_{avg} times, and the resulting FORCs averaged.

3.3. FORC Processing

After simulation, the FORCs were imported into FORCinel [*Harrison and Feinberg*, 2008] and processed using the VARIFORC method [*Egli*, 2013]. Prior to processing, the lower branch of the hysteresis loop was subtracted from each FORC to produce a set of "difference FORCs." Subtracting the lower branch has no effect on the FORC distribution, but does dramatically reduce the presence of common processing artifacts. This procedure, recommended by *Egli* [2013], eliminates sigmoidal contributions to the FORCs near the remanence diagonal, which cannot be described by the second-order polynomial function used to smooth the FORC surface. Although originally conceived to account for superparamagnetic contributions to experimental FORC diagrams, we found this procedure also improved the processing of the simulated FORC diagrams.

4. Results

In the following sections, we compare simulated FORC diagrams for a number of geometries of relevance to rock magnetism. To aid comparison, all simulations have been performed using the same input parameters for particle volume (particles are modeled as 100 nm diameter spheres with volume 523,600 nm^3) and saturation magnetization ($M_s = 480$ kA/m: equivalent to magnetite at room temperature). All simulations have been performed using a lognormal distribution of anisotropy values, such that the probability density of a particle being assigned a given value of B_{Ki} is:

$$\rho(B_{Ki}) = \frac{1}{\sigma\sqrt{2\pi}}\exp\left[-\frac{1}{2}\left(\frac{\ln(\beta B_{Ki})}{\sigma}\right)^2\right] \tag{15}$$

where σ is the width parameter of the corresponding normal distribution in log-space and β is a scaling factor. Values of $\sigma = 0.5$ and $\beta = 20$ were used for all simulations, which produces a distribution spanning the range of coercivities typically encountered in magnetite-bearing rocks.

4.1. Random Packing of Uniaxial Particles: Quasi-Static Approach

FORC diagrams for randomly packed, randomly oriented ensembles of uniaxial particles with a range of packing fractions were simulated using the quasi-static Stoner-Wohlfarth approach (Figure 1). The
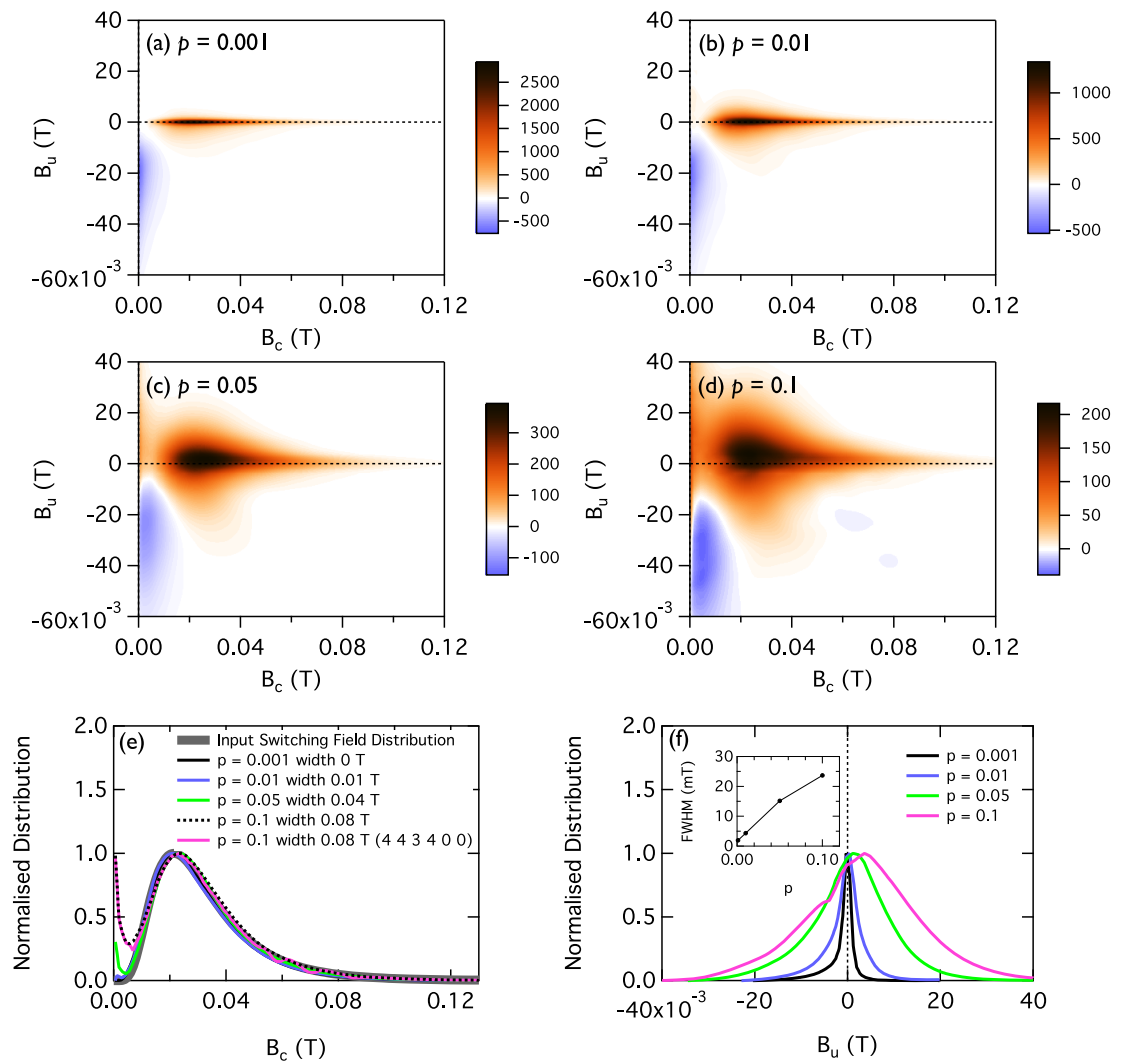
Figure 1. Quasi-static Stoner-Wohlfarth simulation for randomly packed, randomly oriented, uniaxial particles. (a) Simulation parameters: $p = 0.001$, $N = 1000$, $N_{avg} = 100$, $N_{FORC} = 100$, $B_c = 130$ mT, $B_u = 20$ mT, $\Delta B = 1.5$ mT. VARIFORC smoothing parameters: $\{s_{c0}, s_{c1}, s_{b0}, s_{b1}, \lambda_c, \lambda_b\} = \{3, 7, 2, 7, 0.1, 0.1\}$. (b) Simulation parameters: $p = 0.01$, $N = 1000$, $N_{avg} = 100$, $N_{FORC} = 100$, $B_c = 130$ mT, $B_u = 20$ mT, $\Delta B = 1.5$ mT. VARIFORC smoothing parameters: $\{s_{c0}, s_{c1}, s_{b0}, s_{b1}, \lambda_c, \lambda_b\} = \{3, 7, 2, 7, 0.1, 0.1\}$. (c) Simulation parameters: $p = 0.05$, $N = 1000$, $N_{avg} = 200$, $N_{FORC} = 100$, $B_c = 160$ mT, $B_u = 60$ mT, $\Delta B = 2.5$ mT. VARIFORC smoothing parameters $\{s_{c0}, s_{c1}, s_{b0}, s_{b1}, \lambda_c, \lambda_b\} = \{4, 7, 3, 7, 0.1, 0.1\}$. (d) Simulation parameters: $p = 0.1$, $N = 1000$, $N_{avg} = 100$, $N_{FORC} = 100$, $B_c = 160$ mT, $B_u = 60$ mT, $\Delta B = 2.5$ mT. VARIFORC smoothing parameters $\{s_{c0}, s_{c1}, s_{b0}, s_{b1}, \lambda_c, \lambda_b\} = \{4, 7, 3, 7, 0.1, 0.1\}$. (e) Horizontal profiles at $B_u = 0$. The profiles were obtained by summing the FORC distribution inside a window of specified width, centered on the $B_u = 0$ axis, and normalizing to the peak value. The input distribution of switching fields, assuming randomly oriented particles with a lognormal distribution of B_{Ki} (equation (15) with $\sigma = 0.5$ and $\beta = 20$) is shown as the solid gray curve. The values (4 4 3 4 0 0) refer to a different set of VARIFORC smoothing parameters used for that profile. (f) Vertical profiles at $B_c = 20$ mT. Inset shows the FWHM of the vertical profile as a function of packing fraction (p).

corresponding raw FORCs and difference FORCs are presented in the supporting information (Figure S1). For the purposes of avoiding particle overlap, each particle is assumed to be spherical. We define the packing fraction, p, as:

$$p = \frac{1}{L^3} \sum_{i=1}^{N} V_i \qquad (16)$$

where L is the dimension of the cubic space in which the particles are randomly placed.

For $p = 0.001$ (Figure 1a), magnetostatic interactions are extremely weak and the FORC diagram shows the expected features of randomly oriented, noninteracting Stoner-Wohlfarth particles [*Newell*, 2005]: (i) a central ridge along the $B_u = 0$ axis, (ii) positive and negative background signals for $B_u < 0$, and (iii) no signal for

$B_u > 0$. A horizontal line profile of the FORC distribution along the central ridge is shown in Figure 1e, and follows closely the input distribution of switching fields. A vertical line profile taken at $B_c = 0.02$ T, close to the peak of the FORC distribution, produces a sharp asymmetric peak (Figure 1f). Although the finite width of the peak might, at first, be interpreted as a measure of weak interactions between the particles, the full width at half maximum (FWHM) of the peak (1.9 mT; see inset to Figure 1f) is only just above field resolution of the simulation ($\Delta B = 1.5$ mT), and is much wider than the actual interaction-field distribution at this packing fraction. The need for high-resolution measurements to reveal the true nature of the central ridge in noninteracting systems is discussed by *Egli et al.* [2010]; the same principles apply to simulations. For consistency, the field steps used here were chosen so that all simulations used a standard number of FORCs ($N_{FORC} = 100$) to cover the required region of FORC space. Smaller field steps are recommended when using *FORCulator* to study the finer details of the central ridge.

With increasing packing fraction, the central ridge becomes broadened into the horizontal "teardrop" shape predicted by *Egli* [2006] (Figures 1b–1d). The teardrop shape is significant, as it differs considerably from the elliptical shape predicted by classical Preisach theory (obtained here using the static approximation—see supporting information Figure S2). The teardrop becomes increasingly asymmetric about the $B_u = 0$ axis with increasing packing fraction, with the lower half developing into a "lobe" flanked by a strong negative signal to its left and a weak (but statistically significant) negative signal to its right. Such lobes are a characteristic feature of strongly interacting systems [*Evans et al.*, 2006; *Miot et al.*, 2014]. Vertical line profiles close to the peak of the FORC distribution show both a broadening and a shift to positive B_u (Figure 1f). Due to the broadening, horizontal line profiles now need to be integrated vertically in order to obtain a good estimate of the switching field distribution (Figure 1e). The choice of integration window is a compromise between capturing as much of the teardrop as possible whilst avoiding as much of the negative signal as possible (which distorts the distribution for small B_c). A slight difference between the input switching field distribution and the horizontal FORC profile was observed for $p = 0.1$ (dotted curve in Figure 1e). This discrepancy was removed by using a smaller smoothing factor (pink curve in Figure 1e), highlighting the importance of not oversmoothing FORC diagrams when performing quantitative analysis. The limits of the quasi-static approach become increasingly evident for $p \geq 0.05$, with the emergence of oscillatory behavior in the magnetization curves and a vertically spread positive contribution to the FORC diagram close to the $H_c = 0$ axis (Figures 1c and 1d). For $p > 0.1$, results become physically unrealistic, as illustrated by the nonequilibrium form of the FORC diagram for $p = 0.15$ (supporting information Figure S3).

4.2. Random Packing of Uniaxial Particles: Approximate LLG Approach
FORC diagrams for randomly packed, randomly oriented ensembles of uniaxial particles with a range of packing fractions were simulated using the approximate LLG approach (Figure 2). The corresponding raw FORCs and difference FORCs are presented in the supporting information (Figure S4). Results for $p < 0.01$ are equivalent to those obtained using the quasi-static approach. The asymmetric teardrop (Figure 2a) and interaction lobe (Figure 2b) develop for $p > 0.01$, but not the vertically spread positive contribution to the FORC diagram close to the $H_c = 0$ axis that was observed in the quasi-static calculations (Figures 1c and 1d). For $p > 0.2$, the peak evolves from a teardrop into an ellipse (Figure 2c), and becomes stretched along the vertical B_u axis with increasing p (Figure 2d). At these large packing fractions, the FORC diagram resembles the "wishbone" structure, characteristic of perpendicular recording media [*Pike et al.*, 2005; *Dobrotă and Stancu*, 2013]. Horizontal profiles again follow closely the input distribution of switching fields (Figure 2e), although for $p \geq 0.3$ there is a small systematic overestimate of the distribution in the coercivity range 0.06–0.12 T, which was not removed by using smaller smoothing factors. A linear increase in the FWHM of vertical profiles through the peak distribution with p is observed (Figure 2f inset). A least squares fit to the FWHM data yielded an intercept of 3 ± 1 mT (i.e., just above the $\Delta B = 2.5$ mT field step size of the simulation) and slope 180 ± 8 mT.

Values of the saturation magnetization (M_s), saturation remanence (M_{rs}), coercivity (B_c), and coercivity of remanence (B_{cr}) were extracted from the raw FORCs and are plotted in Figure 3a in the form of a "Day plot" of M_{rs}/M_s versus B_{cr}/B_c. The results are consistent with previous studies using micromagnetic simulations of regularly spaced particles [*Muxworthy*, 2003]. The ensemble moves from the SD field into the PSD field, following a distinct curved path that extrapolates to the MD field. The path taken resembles the "mixing paths" defined by *Dunlop* [2002a] for mixtures of noninteracting SD and MD particles.
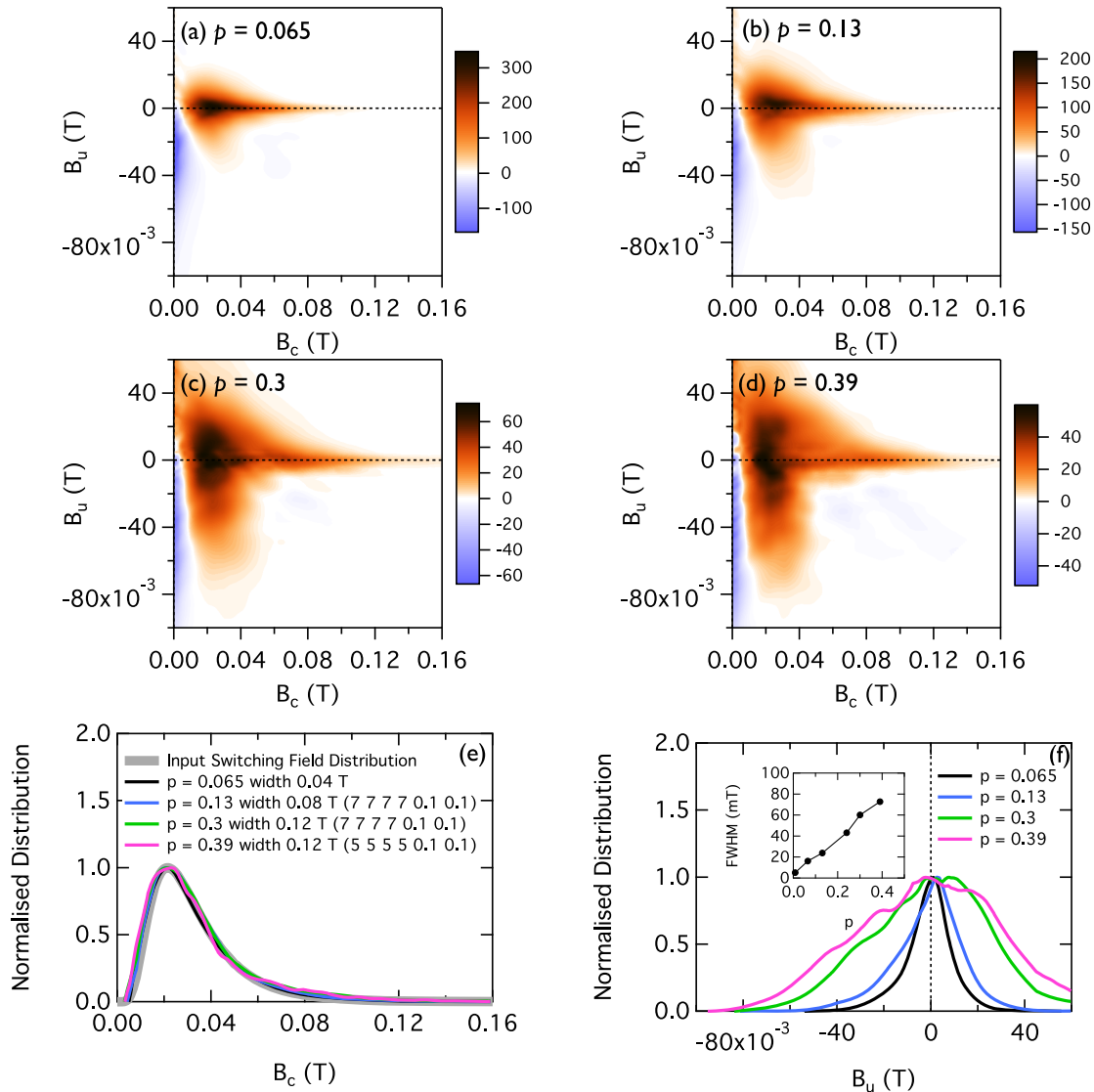
Figure 2. LLG simulations for randomly packed, randomly oriented, uniaxial particles. (a) Simulation parameters: $p = 0.065$, $N = 1000$, $N_{avg} = 25$, $N_{FORC} = 100$, $B_c = 160$ mT, $B_u = 60$ mT, $\Delta B = 2.5$ mT. VARIFORC smoothing parameters: $\{s_{c0}, s_{c1}, s_{b0}, s_{b1}, \lambda_c, \lambda_b\} = \{3, 7, 3, 7, 0.2, 0.2\}$. (b) Simulation parameters: $p = 0.13$, $N = 1000$, $N_{avg} = 25$, $N_{FORC} = 100$, $B_c = 160$ mT, $B_u = 60$ mT, $\Delta B = 2.5$ mT. VARIFORC smoothing parameters: $\{s_{c0}, s_{c1}, s_{b0}, s_{b1}, \lambda_c, \lambda_b\} = \{3, 7, 4, 7, 0.2, 0.2\}$. (c) Simulation parameters: $p = 0.3$, $N = 1000$, $N_{avg} = 25$, $N_{FORC} = 100$, $B_c = 160$ mT, $B_u = 60$ mT, $\Delta B = 2.5$ mT. VARIFORC smoothing parameters: $\{s_{c0}, s_{c1}, s_{b0}, s_{b1}, \lambda_c, \lambda_b\} = \{3, 7, 4, 7, 0.2, 0.2\}$. (d) Simulation parameters: $p = 0.39$, $N = 1000$, $N_{avg} = 25$, $N_{FORC} = 100$, $B_c = 160$ mT, $B_u = 60$ mT, $\Delta B = 2.5$ mT. VARIFORC smoothing parameters: $\{s_{c0}, s_{c1}, s_{b0}, s_{b1}, \lambda_c, \lambda_b\} = \{3, 7, 6, 7, 0.2, 0.2\}$. (e) Horizontal profiles at $B_u = 0$. The profiles were obtained by summing the FORC distribution inside a window of specified width, centered on the $B_u = 0$ axis, and normalizing to the peak value. The input distribution of switching fields, assuming randomly oriented particles with a lognormal distribution of B_{Ki} (equation (15) with $\sigma = 0.5$ and $\beta = 20$) is shown as the solid gray curve. (f) Vertical profiles at $B_c = 25$ mT. Inset shows the FWHM of the vertical profile as a function of packing fraction (p).

4.3. Noninteracting Cubic <111> Particles

Unlike the uniaxial case [*Newell*, 2005], there is no analytical solution for the FORC diagram of noninteracting particles with cubic anisotropy. Although the theoretical hysteresis loop for cubic anisotropy has been computed [*Usov and Peschany*, 1997], the availability of multiple states that a particle can fall into during switching means that a dynamic solution of the LLG equation is required. To our knowledge, the only published micromagnetic calculation of a FORC diagram for particles with cubic anisotropy was performed by *Muxworthy et al.* [2004], who only investigated weakly interacting particles ($p \sim 0.005$). It is worth examining in some detail, therefore, our prediction for noninteracting particles with cubic anisotropy. The FORC diagram, raw FORCs, and difference FORCs for $p = 10^{-5}$ are shown in Figure 4. The bulk hysteresis parameters ($M_{rs}/M_s = 0.864$, $B_c = 9.2$ mT; Figure 4c) are close to the expected theoretical values for randomly oriented
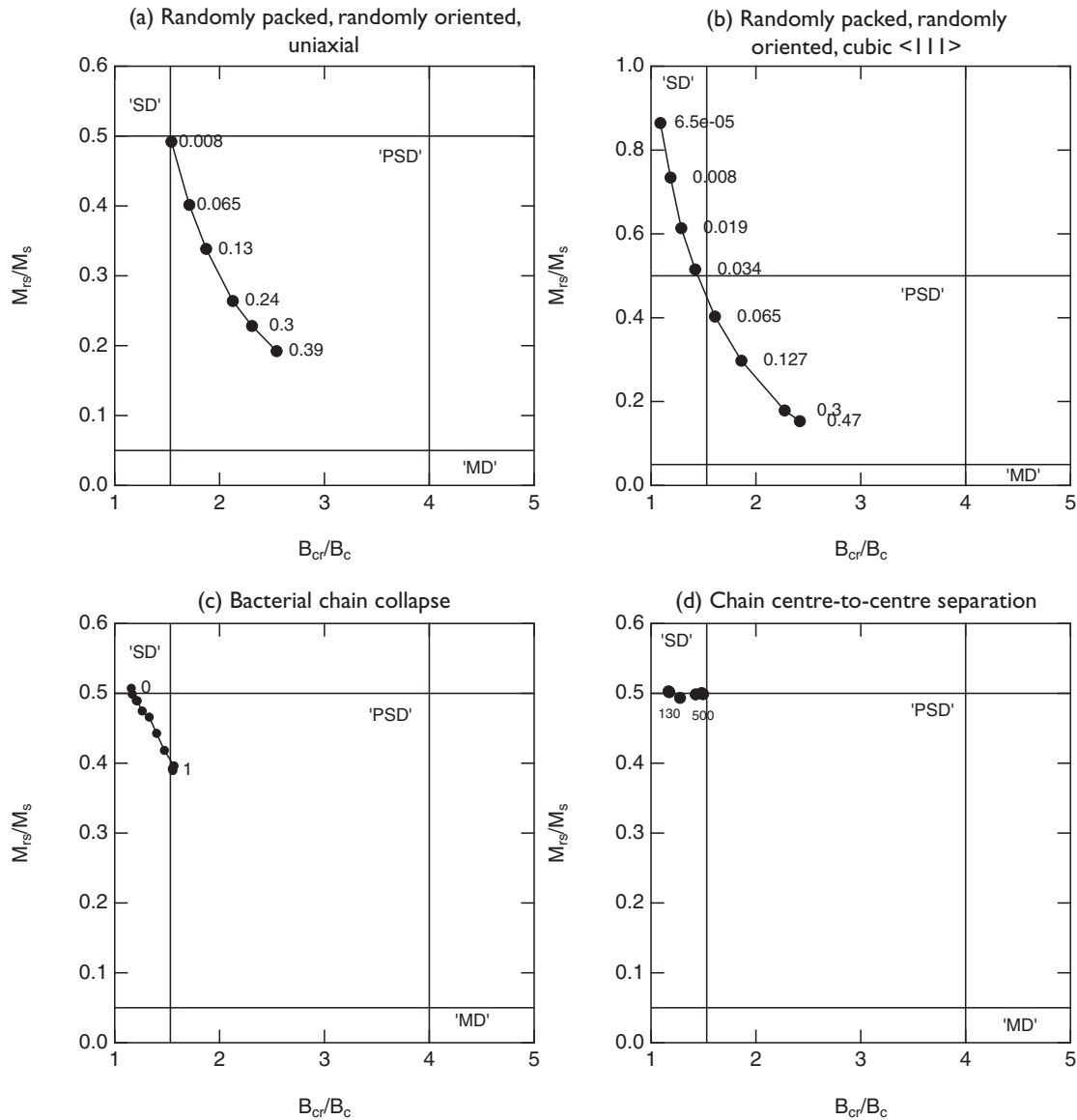
Figure 3. Day plot parameters extracted from the FORC simulations. (a) LLG simulations for randomly packed, randomly oriented, uniaxial particles. Numbers indicate the packing fraction (*p*). (b) LLG simulations for randomly packed, randomly oriented, cubic particles with <111> easy axes. Numbers indicate the packing fraction (*p*). (c) LLG simulation for chains of 100 nm diameter particles and a center-to-center separation of 110 nm as function of chain collapse. Numbers indicate the chain collapse factor (*c*). (d) LLG simulation for chains (*c* = 0.2) of 100 nm diameter particles with increasing particle separation. Numbers indicate the center-to-center separation of the particles (in nm).

particles with cubic <111> anisotropy (i.e., $M_{rs}/M_s = 0.866$ and $0.18\,B_K < B_c < 0.2\,B_K$) [*Usov and Peschany*, 1997]. Note that the peak of the input anisotropy distribution (equation (15)) occurs at $B_K = 50$ mT, so the observed value of $B_c = 9.3$ mT is within the expected range of $9 < B_c < 10$ mT. The FORC diagram (Figure 4a) shares some of the characteristics of the FORC diagram for noninteracting uniaxial particles (Figure 1a): (i) a ridge of intensity close to the $B_u = 0$ axis (labeled "1" in Figure 4b), (ii) positive and negative background signals for $B_u < 0$ (labeled "2" and "3" in Figure 4b), and (iii) no signal for $B_u > 0$. Some key distinguishing features are present, however: (i) the peak of the FORC distribution is displaced slightly (<0.5 mT) to negative B_u values, (ii) a new negative signal appears above the remanence diagonal (labeled "4" in Figure 4b). The origin of signal 4 can best be seen in the difference FORCs (Figure 4d), which all display a pronounced peak in the field range associated with upward switching events. From the color coding in Figure 4d, the negative signal 4 (blue) can be seen to originate from the left flank of this peak, the positive signal 2 (orange) originates from the right flank of the peak, and the ridge signal 1 (black) originates from the point where
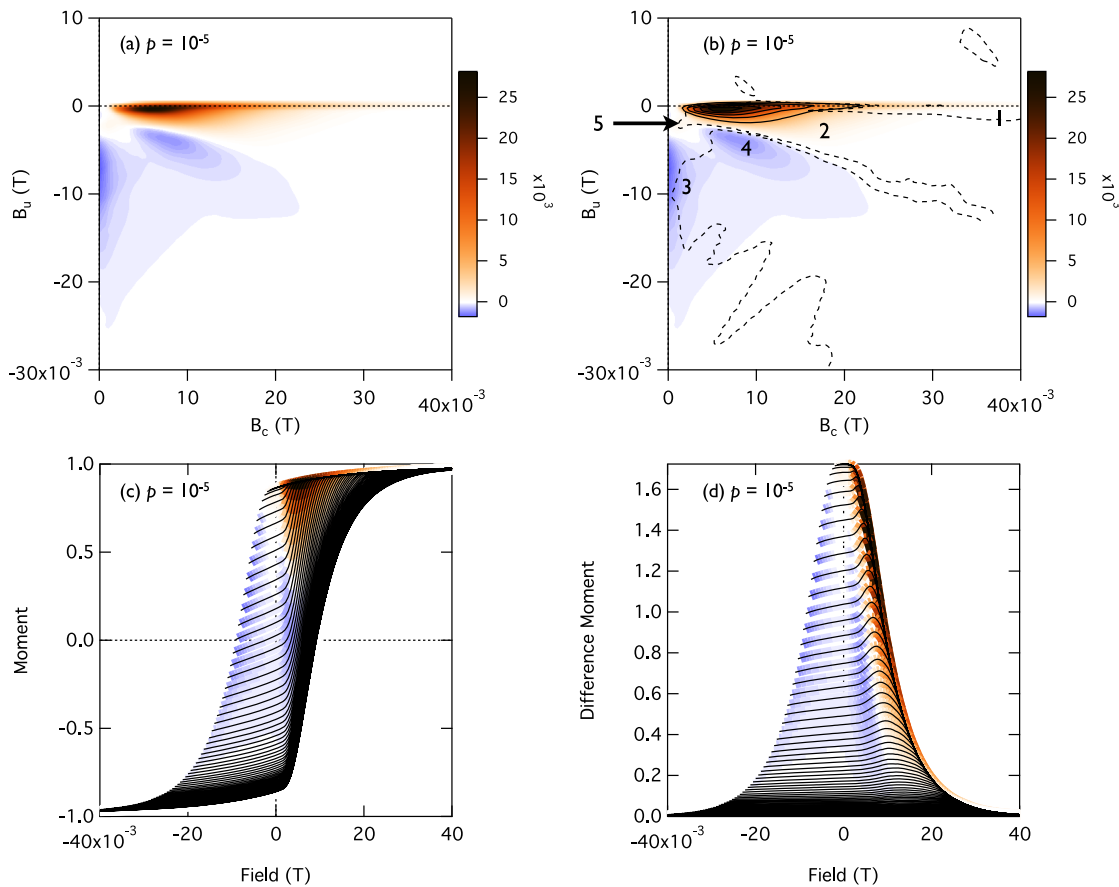
Figure 4. (a) LLG simulation for randomly packed, randomly oriented, cubic particles with <111> easy axes. Simulation parameters: $p = 10^{-5}$ (i.e., noninteracting), $N = 250$, $N_{avg} = 200$, $N_{FORC} = 100$, $B_c = 50$ mT, $B_u = 10$ mT, $\Delta B = 0.6$ mT. VARIFORC smoothing parameters: $\{s_{c0}, s_{c1}, s_{b0}, s_{b1}, \lambda_c, \lambda_b\} = \{3, 7, 2, 7, 0.2, 0.2\}$. (b) Same as Figure 4a but with added contours for the FORC distribution (solid lines) and signal-to-noise threshold of 3 (dashed line). (c) Raw FORCs (black lines) with background colors indicating the corresponding value of the FORC distribution at that point. Colors are plotted according to the same color scale as in Figure 4a. (d) Difference FORCs derived from Figure 4c by subtracting the lowermost FORC from each individual FORC.

each difference FORC intersects the envelope of the upper hysteresis branch. Signal 4 was also seen in the calculation of *Muxworthy et al.* [2004], along with the small region of weak, but statistically significant, positive signal labeled "5" in Figure 4b.

4.4. Random Packing of Cubic <111> Particles

FORC diagrams for randomly packed, randomly oriented ensembles of cubic particles with <111> easy axes and a range of packing fractions were simulated using the approximate LLG approach (Figure 5). The corresponding raw FORCs and difference FORCs are presented in the supporting information (Figure S5). For $p = 0.01$, the main peak broadens into a flattened teardrop shape, retaining the small offset in the negative B_u direction (Figure 5a). The ridge-like signal 1 is retained at higher B_c, but the negative signal 4, and its associated peak in the difference FORCs, are much less pronounced. For $p = 0.035$, the broadening of the peak continues and a positive lobe starts to develop between signals 3 and 4 (Figure 5b). For $p = 0.1$ (Figure 5c), the lobe observed for $B_u < 0$ is fully developed, while the FORC distribution for $B_u > 0$ takes on a more triangular shape, with vertically spreading intensity extending all the way to $B_c = 0$ (contrast this with the closed teardrop shape observed for unixial particles; Figure 2b). For $p = 0.3$ (Figure 5d), the peak becomes vertically stretched into a wishbone structure resembling Figure 2d. Unlike the uniaxial case, strong interactions between cubic particles lead to broadening in both vertical and horizontal directions (Figures 5e and 5f). A linear increase in the FWHM of vertical profiles through the peak distribution with p is observed (Figure 5f inset). A least squares fit to the FWHM data yielded an intercept of 1.3 ± 1 mT (i.e., just above the $\Delta B = 1$ mT field step size of the simulation) and slope 197 ± 3 mT. The corresponding changes in bulk hysteresis parameters are represented on a Day plot in Figure 3b. Again there is a systematic shift of the
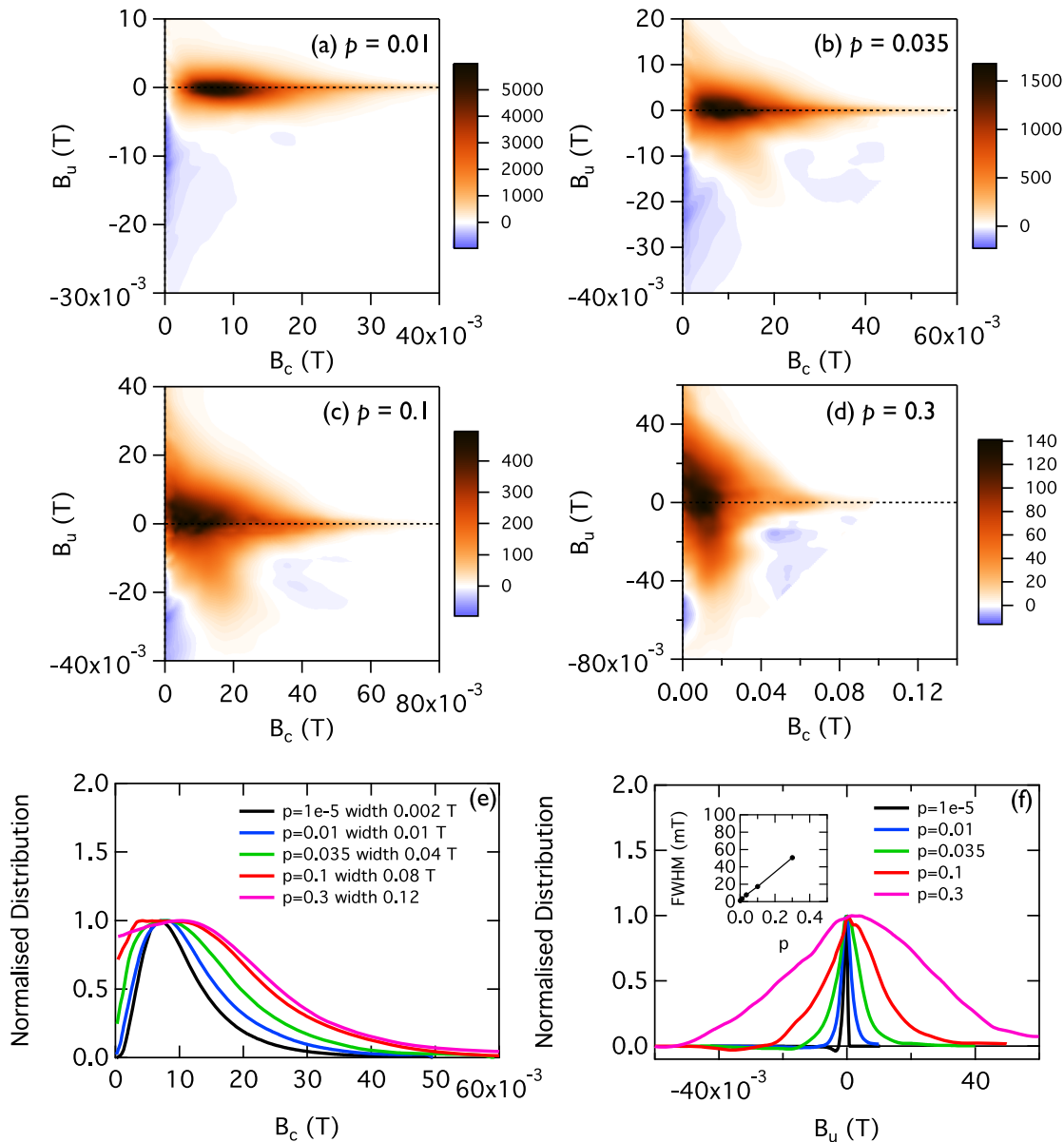
Figure 5. LLG simulations for randomly packed, randomly oriented, cubic particles with <111> easy axes. (a) Simulation parameters: $p = 0.01$, $N = 250$, $N_{avg} = 200$, $N_{FORC} = 100$, $B_c = 50$ mT, $B_u = 10$ mT, $\Delta B = 0.6$ mT. VARIFORC smoothing parameters: $\{s_{c0}, s_{c1}, s_{b0}, s_{b1}, \lambda_c, \lambda_b\} = \{3, 7, 2, 7, 0.2, 0.2\}$. (b) Simulation parameters: $p = 0.035$, $N = 250$, $N_{avg} = 200$, $N_{FORC} = 100$, $B_c = 60$ mT, $B_u = 40$ mT, $\Delta B = 1$ mT. VARIFORC smoothing parameters: $\{s_{c0}, s_{c1}, s_{b0}, s_{b1}, \lambda_c, \lambda_b\} = \{3, 7, 3, 7, 0.2, 0.2\}$. (c) Simulation parameters: $p = 0.1$, $N = 250$, $N_{avg} = 200$, $N_{FORC} = 100$, $B_c = 100$ mT, $B_u = 50$ mT, $\Delta B = 1.5$ mT. VARIFORC smoothing parameters: $\{s_{c0}, s_{c1}, s_{b0}, s_{b1}, \lambda_c, \lambda_b\} = \{3, 7, 3, 7, 0.2, 0.2\}$. (d) Simulation parameters: $p = 0.3$, $N = 250$, $N_{avg} = 200$, $N_{FORC} = 100$, $B_c = 100$ mT, $B_u = 60$ mT, $\Delta B = 1.6$ mT. VARIFORC smoothing parameters: $\{s_{c0}, s_{c1}, s_{b0}, s_{b1}, \lambda_c, \lambda_b\} = \{9, 9, 9, 9, 0.2, 0.2\}$. (e) Horizontal profiles at $B_u = 0$. The profiles were obtained by summing the FORC distribution inside a window of specified width, centered on the $B_u = 0$ axis, and normalizing to the peak value. (f) Vertical profiles at $B_c = 7$ mT. Inset shows the FWHM of the vertical profile as a function of packing fraction (p).

ensemble from the cubic SD field to the uniaxial SD field, into the PSD field and toward the MD field, along a distinct curved path. The speed with which the ensemble moves along this path with increasing packing fraction is greater for the cubic case than for the uniaxial case.

4.5. Chains of Particles: Effect of Chain Collapse

Single chains of particles can be created in *FORCulator* using a constrained, self-avoiding random walk (Figure 6a). The first particle in a chain (p_1) is positioned at random, subject to the constraint that it does not overlap with any particles previously generated in the ensemble. The second particle (p_2) is placed at a specified center-to-center distance, d, from p_1. The vector $\overrightarrow{p_2}$, joining particle p_1 to p_2, can either be chosen
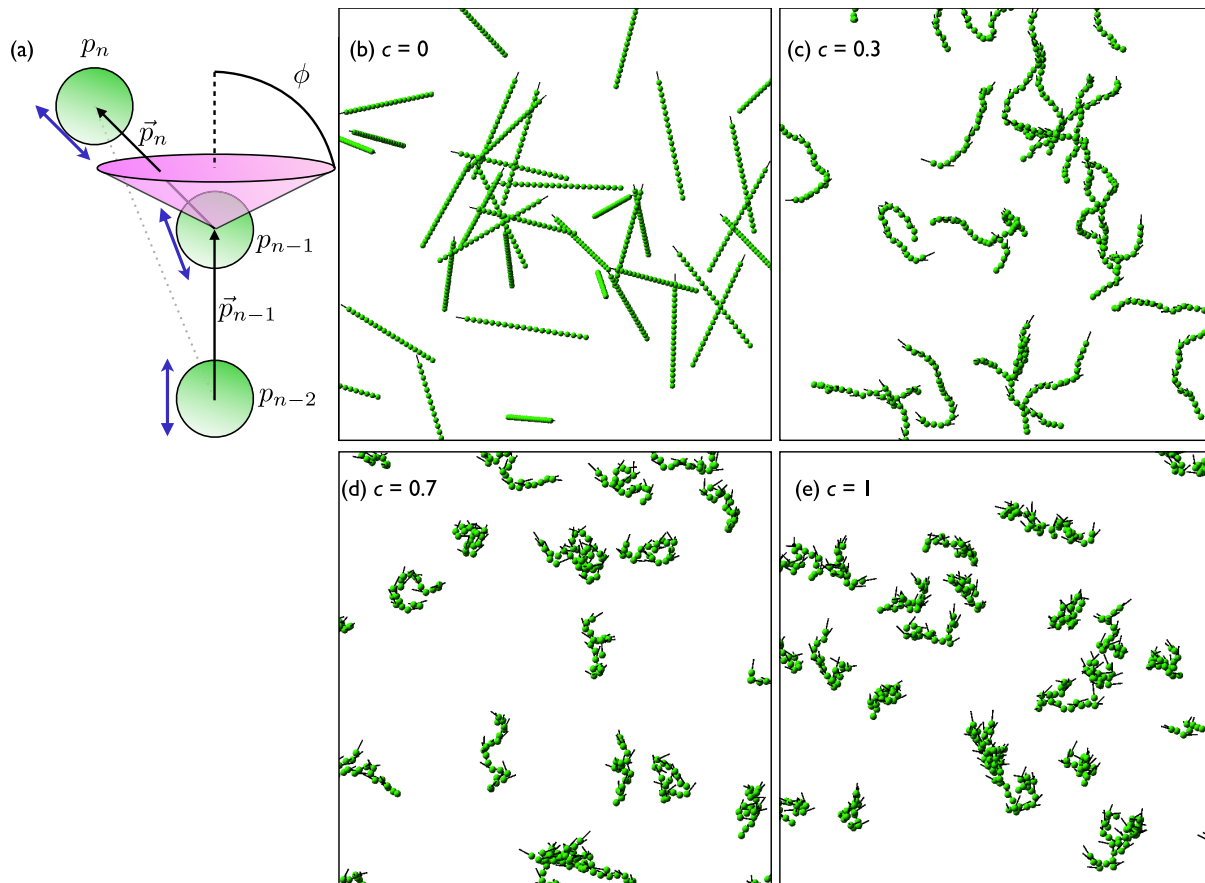
Figure 6. (a) Definition of the method used to generate collapsed particle chains via a constrained self-avoiding random walk. The diagram depicts how the position of the third particle in a three particle chain ($N_p = 3$) is chosen. The vector $\overrightarrow{p_n}$ is selected randomly within a cone of semiangle φ, centered on p_{n-1} and aligned with $\overrightarrow{p_{n-1}}$. The easy axis of a particle inside the chain points along the vector joining the particles immediately before and after it (gray dotted line). The easy axis of particles at the beginning and end of the chain are aligned with the vectors $\overrightarrow{p_2}$ and $\overrightarrow{p_{N_p}}$, respectively. (b–e) Ensembles of chains generated with different collapse factors. Each chain contains 20 spherical particles with diameter 100 nm and a center-to-center distance between particles of 110 nm. Each image represents a magnified portion of an ensemble of 50 randomly aligned chains inside a $10 \times 10 \times 10$ μm box. Black lines show the orientations of uniaxial easy axes, which were constrained to be parallel to the chain axis.

at random or it can be constrained to lie along a specific direction to create a degree of chain alignment. Once the first two particles in a chain have been placed, further particles are added sequentially until the specified number of particles in the chain, N_p, is reached. The nth particle in the chain, p_n, is placed at the end of the vector, $\overrightarrow{p_n}$, joining the centers of particles p_{n-1} and p_n. Candidate orientations are chosen such that there is a uniform probability of $\overrightarrow{p_n}$ falling inside a cone with axis $\overrightarrow{p_{n-1}}$ and semiangle φ (Figure 6a). Acceptance of a candidate orientation of $\overrightarrow{p_n}$ is subject to the constraint that no particle should overlap with any other particle previously generated in the ensemble. To create systematic changes in the degree of chain collapse, we define a chain collapse factor, c ($0 \leq c \leq 1$), such that $\varphi = c\pi$ (Figures 6b–6e). The easy axis orientation of each particle in the chain can either be chosen at random, or it can be chosen to align with the chain axis. Chain axis alignment is achieved by defining the easy axis vector of particle p_{n-1} to be parallel to the vector sum $\overrightarrow{p_{n-2}} + \overrightarrow{p_n}$ (Figure 6a). Easy axes for the first and last particles in the chain are defined to be parallel to $\overrightarrow{p_2}$ and $\overrightarrow{p_{N_p}}$, respectively.

FORC diagrams for randomly packed, randomly oriented chains of uniaxial particles, with easy axes aligned to the chain axis, were simulated using the approximate LLG approach (Figure 7). The corresponding raw FORCs and difference FORCs are presented in the supporting information (Figure S6). Each simulation contained 50 chains inside a $10 \times 10 \times 10$ μm box, with each chain containing 20 spherical particles of 100 nm diameter and a center-to-center distance of 110 nm. These parameters were chosen to mimic chains of closely spaced particles, typical of magnetotactic bacteria [*Bazylinski and Frankel*, 2004]. For $c = 0$ (straight chains; Figure 6b), the FORC diagram displays the characteristics
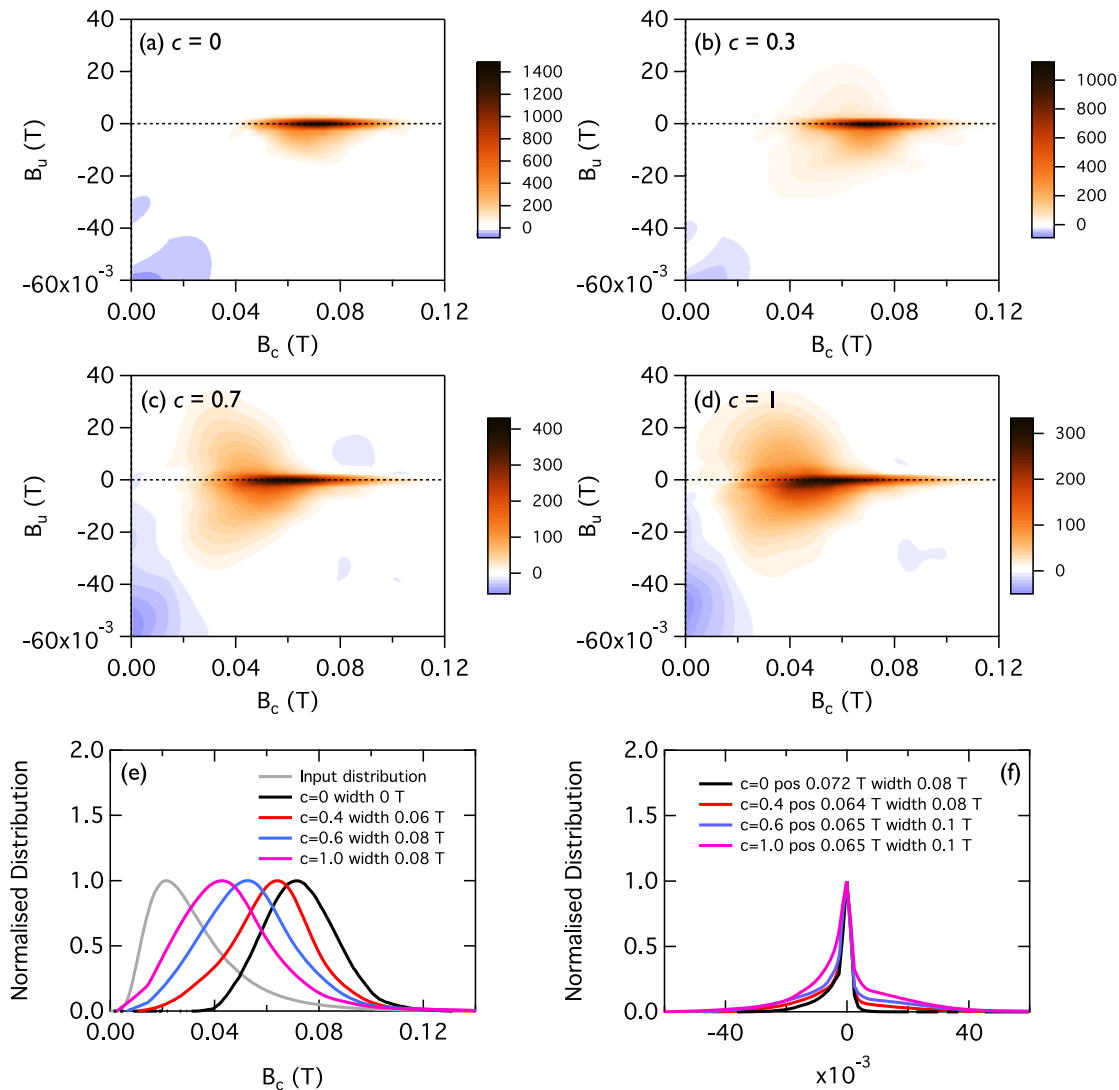
Figure 7. LLG simulations for the chain configurations shown in Figure 6. (a) Simulation parameters: $c = 0$, $N_{avg} = 25$, $N_{FORC} = 100$, $B_c = 160$ mT, $B_u = 60$ mT, $\Delta B = 2.5$ mT. VARIFORC smoothing parameters: $\{s_{c0}, s_{c1}, s_{b0}, s_{b1}, \lambda_c, \lambda_b\} = \{12, 12, 2, 12, 0, 0\}$. (b) Simulation parameters: $c = 0.3$, $N_{avg} = 25$, $N_{FORC} = 100$, $B_c = 160$ mT, $B_u = 60$ mT, $\Delta B = 2.5$ mT. VARIFORC smoothing parameters: $\{s_{c0}, s_{c1}, s_{b0}, s_{b1}, \lambda_c, \lambda_b\} = \{12, 12, 2, 12, 0, 0\}$. (c) Simulation parameters: $c = 0.7$, $N_{avg} = 25$, $N_{FORC} = 100$, $B_c = 160$ mT, $B_u = 60$ mT, $\Delta B = 2.5$ mT. VARIFORC smoothing parameters: $\{s_{c0}, s_{c1}, s_{b0}, s_{b1}, \lambda_c, \lambda_b\} = \{12, 12, 2, 12, 0, 0\}$. (d) Simulation parameters: $c = 1$, $N_{avg} = 25$, $N_{FORC} = 100$, $B_c = 160$ mT, $B_u = 60$ mT, $\Delta B = 2.5$ mT. VARIFORC smoothing parameters: $\{s_{c0}, s_{c1}, s_{b0}, s_{b1}, \lambda_c, \lambda_b\} = \{12, 12, 2, 12, 0, 0\}$. (e) Horizontal profiles at $B_u = 0$. The profiles were obtained by summing the FORC distribution inside a window of specified width, centered on the $B_u = 0$ axis, and normalizing to the peak value. (f) Vertical profiles taken at the indicated position (corresponding to the peak position of the corresponding horizontal profile) and summed over a window with the specified width.

of noninteracting uniaxial particles (Figure 7a), albeit with a coercivity distribution that is very different to the input distribution (Figure 7e).

For $c = 0.3$, the chain structure remains readily identifiable, but chains are no longer straight and occasionally double back on themselves (Figure 6c). The FORC diagram retains a sharp central ridge, with weak "wings" of intensity developing above and below it. The wings are not centered on the peak of the central-ridge distribution, but displaced significantly to lower B_c values. For $c = 0.7$, the chains are in a partially collapsed state, with many appearing as clusters but with a significant fraction still recognizable as bent chains (Figure 6d). The FORC diagram retains a sharp central ridge, with the wings increasing in intensity. The combination of sharp ridge and distinct wings creates a distinctive "concord" shaped FORC distribution. For $c = 1$, the chains are in their most collapsed state (or, at least, the most collapsed state that can be generated using this algorithm), with the majority appearing as clusters and a small minority retaining some recognizable chain structure (Figure 6e). Again, the central ridge is retained at high coercivity and the low-

HARRISON AND LASCU
4684

coercivity wings, which now form an almost circular pattern, increase in intensity, leading to an apparently bimodal FORC distribution (Figure 7d).

Horizontal profiles through the central ridge show a systematic shift to lower B_c values with increasing chain collapse (Figure 7e), as well the development of low-coercivity shoulders associated with the developing wings. Vertical profiles centered on the peak of the central ridge, but integrated across a wide range of coercivities, show a systemic increase in the intensity of the wings with increasing chain collapse (Figure 7f).

Day plot parameters for collapsed chains move along a relatively straight line within the SD field, with the M_{rs}/M_s ratio decreasing from 0.5 to a minimum value of just under 0.4 for fully collapsed chains (Figure 3c). The values of the B_{cr}/B_c ratio are overall lower than in the case of isolated particles, in part due to higher B_c values. The fact that the ensemble evolves with increasing collapse along a different path from the one followed by randomly packed particles (Figure 3a) is to be expected because of the nonrandom nature of the algorithm used here to generate chain collapse.

4.6. Chains of Particles: Effect of Interparticle Separation

FORC diagrams for randomly packed, randomly oriented chains of uniaxial particles ($c = 0.2$), with easy axes aligned to the chain axis and a range of interparticle separations (d) were simulated using the approximate LLG approach (Figure 8). The corresponding raw FORCs and difference FORCs are presented in the supporting information (Figure S7). Each simulation contained 50 chains inside a $4 \times 4 \times 12$ μm box, with each chain containing 20 spherical particles of 100 nm diameter. Several key changes to the FORC diagram are observed as the interparticle spacing is increased from $d = 110$ nm (as used in the previous section) to $d = 130$ nm (Figure 8a): (i) the peak of the coercivity distribution shifts from $B_c = 0.07$ T to $B_c = 0.053$ T, (ii) the upper wing of intensity associated with the small degree of chain collapse (Figure 7) becomes weaker, (iii) the main peak starts to develop a "boomerang" shape with peak offset to negative B_u, and (iv) a negative signal starts to develop below the boomerang. The lowering of the coercivity, the development of the boomerang shape, the magnitude of the negative offset and the intensity of the negative region become more pronounced with increasing d up to a value of $d = 200$ nm (Figures 8b and 8c). Further increases in d lead to further decreases in coercivity but a reduction in the other features (Figure 8d). By $d = 500$ nm, the FORC diagram resembles that of the equivalent noninteracting case (Figure 1a), although the coercivity distributions are not identical due to the nonrandom easy axis alignment of the chains.

In the Day plot, the ensemble moves from left to right along the $M_{rs}/M_s = 0.5$ line (Figure 3d). The higher values of B_{cr}/B_c with increasing particle separation reflect the evolution of the system from particles arranged in chain structures toward random packing. A center-to-center distance of more than 500 nm is essentially equivalent to random packing with no magnetostatic interactions between particles (Figure 3a).

5. Discussion

5.1. Randomly Packed Particles

The limitations of the quasi-static approach for randomly packed particles are clearly illustrated by the appearance of oscillatory behavior in individual FORCs (Figure S3), the asymmetry of the difference FORC plot about the $B = 0$ axis (Figure S3), and the appearance of an anomalous vertically spread positive contribution to the FORC diagram close to the $H_c = 0$ axis (Figures 1c and 1d). These features are artifacts associated with the breakdown of the assumption that particles undergo independent switching events in a static interaction field and a failure of the simulation to reach the correct equilibrium state. When interactions are strong, the magnetic state of neighboring particles become correlated, and switching events can no longer be considered to be independent. As soon as these effects become significant, an iterated approach is required to find the equilibrium micromagnetic state of the ensemble. These problems are solved by using the approximate iterated LLG approach (Figure 2), albeit at the expense of longer computation times. The LLG approach is recommended for all but the most weakly interacting systems.

Calculated FORC diagrams for interacting particles agree well with those observed experimentally, e.g., in intergrowths [*Evans et al.*, 2006] and clusters of single-domain magnetite [*Miot et al.*, 2014]. The main discrepancy is the larger value of the negative signal observed along the negative B_u axis in the simulated diagrams, which is typically less pronounced or absent in experimental diagrams. The negative signal in experimental diagrams may be suppressed by thermal fluctuations (which are neglected at present in
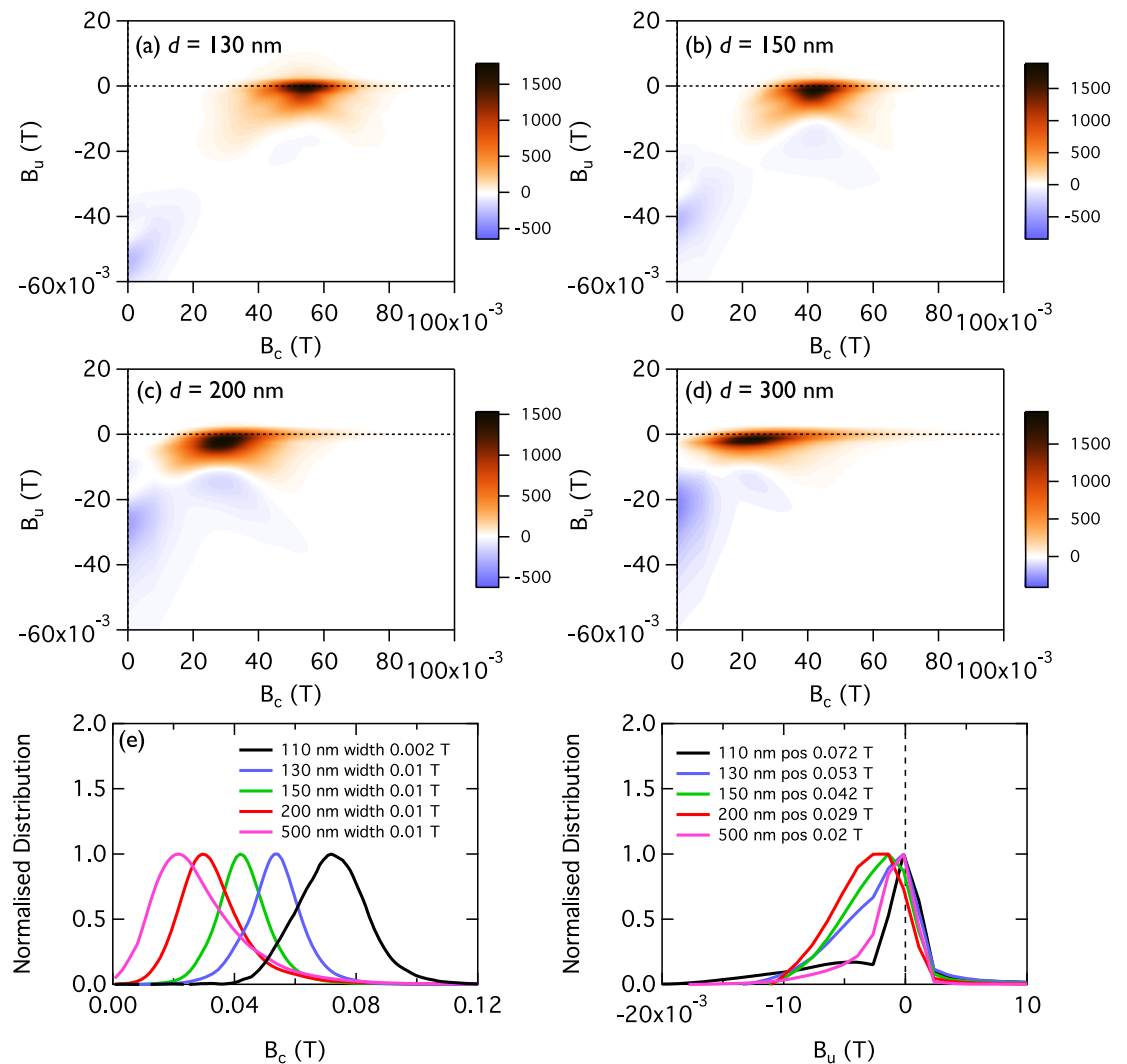
Figure 8. LLG simulations for the chains with a collapse factor of $c = 0.2$ and increasing interparticle separation (d). Chains were oriented at random inside a box of size $4 \times 4 \times 12$ μm. (a) Simulation parameters: $d = 130$ nm, $N_{avg} = 25$, $N_{FORC} = 100$, $B_c = 160$ mT, $B_u = 60$ mT, $\Delta B = 2.5$ mT. VARIFORC smoothing parameters: $\{s_{c0}, s_{c1}, s_{b0}, s_{b1}, \lambda_c, \lambda_b\} = \{7, 7, 2, 7, 0, 0\}$. (b) Simulation parameters: $d = 150$ nm, $N_{avg} = 25$, $N_{FORC} = 100$, $B_c = 160$ mT, $B_u = 60$ mT, $\Delta B = 2.5$ mT. VARIFORC smoothing parameters: $\{s_{c0}, s_{c1}, s_{b0}, s_{b1}, \lambda_c, \lambda_b\} = \{7, 7, 2, 7, 0, 0\}$. (c) Simulation parameters: $d = 200$ nm, $N_{avg} = 25$, $N_{FORC} = 100$, $B_c = 160$ mT, $B_u = 60$ mT, $\Delta B = 2.5$ mT. VARIFORC smoothing parameters: $\{s_{c0}, s_{c1}, s_{b0}, s_{b1}, \lambda_c, \lambda_b\} = \{7, 7, 2, 7, 0, 0\}$. (d) Simulation parameters: $d = 300$ nm, $N_{avg} = 25$, $N_{FORC} = 100$, $B_c = 160$ mT, $B_u = 60$ mT, $\Delta B = 2.5$ mT. VARI-FORC smoothing parameters: $\{s_{c0}, s_{c1}, s_{b0}, s_{b1}, \lambda_c, \lambda_b\} = \{7, 7, 2, 7, 0, 0\}$. (e) Horizontal profiles at $B_u = 0$. The profiles were obtained by summing the FORC distribution inside a window of specified width, centered on the $B_u = 0$ axis, and normalizing to the peak value. (f) Vertical profiles taken at the indicated position (corresponding to the peak position of the corresponding horizontal profile).

FORCulator), or masked by positive contributions to the FORC diagram in that region, e.g., from superparamagnetic or multidomain contributions [*Newell*, 2005].

A key observation is that, even for weakly interacting particles, the form of the FORC diagram differs greatly from that obtained using the standard Preisach assumption of a static interaction field (Figure S2). A major consequence of this is that it is not possible to use the FORC diagram directly as the source of an input Preisach distribution for the purposes of simulating the acquisition of thermoremanent magnetization (TRM), except perhaps in the most weakly interacting cases [*Muxworthy and Heslop*, 2011; *Muxworthy et al.*, 2011; *Lappe et al.*, 2013]. A more robust approach would be to perform an inverse analysis on the FORC diagram to obtain a physical parameterization of the particle ensemble in terms of its coercivity distribution and packing fraction, and then use this physical model of the system as the basis for simulating the acquisition of TRM. The broadening of vertical FORC profiles with packing fraction provides a starting point for such analysis (Figures 2f and 5f). *Egli* [2006] argued that the best method for characterizing the broadening is to
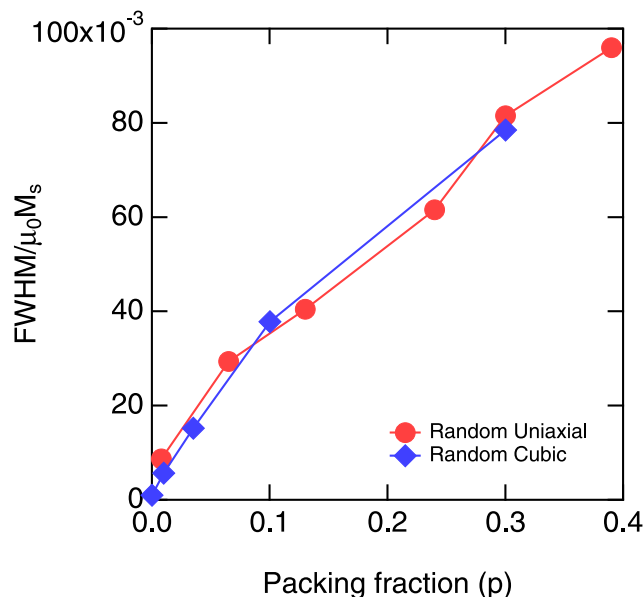
Figure 9. Scaled FWHM, i.e., FWHM (in T) divided by $\mu_0 M_s$ for magnetite (0.603 T), extracted from low-coercivity vertical profiles for randomly packed uniaxial (circles) and cubic (diamonds) particles as a function of packing fraction (*p*). Profiles were taken at coercivities of 10 and 7 mT for uniaxial and cubic particles, respectively. FWHM was defined in this case as twice the half width to half maximum extracted from the upper half (i.e., $B_u > 0$) of the vertical profile.

focus on the upper half (i.e., $B_u > 0$) of vertical profiles taken as far as possible to the left of the central peak. Profiles taken here sample the complete interaction-field distribution seen by a few particles with minimum anisotropy, and by using only the upper half of the profile to define the width, the distorting influence of the negative region can be avoided. Figure 9 shows the dependence of FWHM (defined here as twice the half width at half maximum) divided by $\mu_0 M_s$ derived from the upper half of low-coercivity profiles for randomly packed uniaxial and cubic particles. Note that both uniaxial and cubic particles lie on the same curve and that the nonlinearity is consistent with theoretical predictions [*Egli*, 2006]. Assuming random packing of particles and an appropriate value for M_s, Figure 9 can provide estimates of packing fractions directly from FORC diagrams. For uniaxial particles, the input coercivity distribution is matched closely by horizontal profiles through the FORC distribution (Figure 2e), so this too can be determined directly from the data. This is not possible for strongly interacting particles with cubic anisotropy, however, since horizontal profiles through the FORC distribution do not correspond to the input coercivity distribution (Figure 5e).

Increasing interactions between SD particles moves the system smoothly from the SD into the PSD region of a Day plot (Figures 3a and 3b). Simultaneously, the simulated FORC diagrams start to develop many of the features observed in the FORC diagrams of "true" PSD particles (i.e., noninteracting particles with sizes that are intermediate between those of SD and MD particles). A typical example of a PSD FORC is shown in Figure 10a, which was measured on a sample of fire obsidian from Glass Buttes, Oregon containing particles of magnetite in the PSD size range [*Ma et al.*, 2007]. A comparison of Figure 10a with Figures 2c and 5c reveals many shared features, including the asymmetric vertical broadening about the $B_u = 0$ axis and the development of a lower "lobe" flanked by a negative signal to its left and a weaker (but statistically significant) negative signal to its right. This raises several interesting questions: (i) Can strongly interacting clusters of SD particles be distinguished unambiguously from noninteracting ensembles of PSD particles using FORC diagrams? (ii) Does the high-field isothermal behavior of strongly interacting clusters of SD particles provide a good physical analog to the high-field isothermal behavior of PSD particles? (iii) Does this analog also extend to the low-field, high-temperature behavior of PSD particles? If the answer to the first question is "no," this presents a significant barrier for the development of an inverse method for FORC diagrams. However, if the answer to the latter two questions is "yes," this barrier becomes irrelevant (i.e., if PSD particles are equivalent to strongly interacting particles in terms of the their rock magnetic behavior, then it is no longer necessary to distinguish them from each other for the purpose of modeling). This equivalence could provide a way forward in the modeling of PSD TRM, for which there is currently no practical theory that can be applied in paleomagnetic studies. Examination of the equivalence (or otherwise) between PSD particles and strongly interacting SD clusters will be an important area of future research.

5.2. Chains of Particles

Single or multiple chains of strongly interacting magnetic particles are present in all species of magnetotactic bacteria [*Bazylinski and Frankel*, 2004]. The linear arrangement of magnetosomes along the chain axis is biologically controlled by means of a proteinous filament [*Faivre and Schüler*, 2008] in order to optimize the
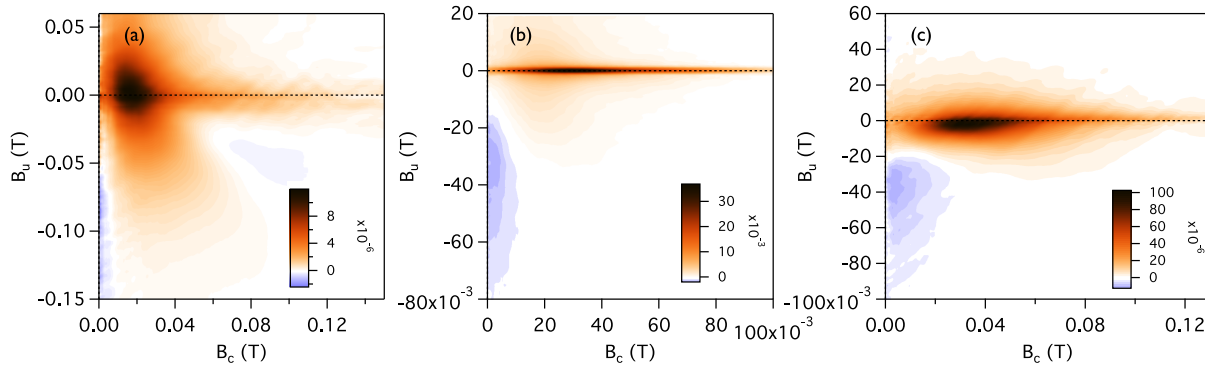
Figure 10. FORC diagrams of natural samples: (a) fire obsidian from Glass Buttes, Oregon containing PSD magnetite. Measurement parameters: B_{sat} = 1.7 T, B_c = 150mT, B_u = 60 mT, ΔB = 1 mT, t_{avg} = 100 ms, N_{FORC} = 283. VARIFORC smoothing parameters: {s_{c0}, s_{c1}, s_{b0}, s_{b1}, λ_c, λ_b} = {9, 9, 9, 0.2, 0.2}; (b) sediment from Brownie Lake Minnesota containing magnetosomes. Measurement parameters: B_{sat} = 0.2 T, B_c = 110 mT, B_u = 15 mT, ΔB = 0.83 mT, t_{avg} = 500 ms, N_{FORC} = 182. VARIFORC smoothing parameters: {s_{c0}, s_{c1}, s_{b0}, s_{b1}, λ_c, λ_b} = {6, 6, 3, 6, 0.1, 0.1}; (c) Olivine crystal containing magnetite precipitated along dislocations. Measurement parameters: B_{sat} = 2.2 T, B_c = 130 mT, B_u = 50 mT, ΔB = 0.75 mT, t_{avg} = 200 ms, N_{FORC} = 293. VARIFORC smoothing parameters: {s_{c0}, s_{c1}, s_{b0}, s_{b1}, λ_c, λ_b} = {5, 7, 4, 7, 0.1, 0.1}.

magnetic properties of the chain for the purposes of magnetotaxis. Post mortem, however, the cell structure will undergo lysis (i.e., breakdown), leading to varying degrees of chain collapse during diagenesis [*Li et al.*, 2012]. Similar effects can be seen by genetically modifying bacteria to remove the biological structures necessary to maintain chain integrity [*Faivre and Schüler*, 2008]. FORC diagrams have emerged as a powerful tool to detect the presence of magnetotactic bacteria and magnetofossils in sediments [*Egli et al.*, 2010; *Roberts et al.*, 2012; *Heslop et al.*, 2014]. There is considerable interest, therefore, in exploring the FORC signatures associated with varying degrees of chain collapse [*Chen et al.*, 2007; *Li et al.*, 2012].

The FORC diagram of perfectly straight chains (Figure 7a) illustrates the dominance of intrachain magnetostatic interactions over the properties of individual magnetosomes in determining the switching properties of the chain. Unlike the FORC diagram in Figure 1a, which is consistent with the prediction of *Newell* [2005] for an ensemble of randomly oriented, noninteracting uniaxial particles with a lognormal distribution of switching fields, the FORC diagram in Figure 7a is closer to the theoretical prediction for an ensemble of randomly oriented, noninteracting uniaxial particles with *identical* switching fields [*Newell*, 2005]. The theoretical FORC distribution for identical particles with intrinsic switching field B_K is zero for $B_c < 0.5B_K$, is asymptotic to infinity at $B_c = 0.5B_K$ and drops rapidly to zero at $B_c = B_K$. Here we observe an approximately Gaussian peak at $B_c = 0.07$ T, which is close to half of the highest statistically significant value of coercivity ($B_c = 0.12$ T). The observed distribution is zero below $B_c = 0.04$ T, despite the majority of particles having intrinsic switching fields below this value (Figure 7e). From this we can conclude that straight chains act as individual switching units, and that the intrinsic switching field of a chain is close to the switching field of the most coercive particle within it.

The peak of the coercivity distribution shifts to lower values with increasing chain collapse, but does not reach the input distribution of coercivities of individual particles, even for fully collapsed chains. In addition, the bimodality of the coercivity distribution, which is most apparent for fully collapsed chains, is similar to that of coercivity distributions that contain a mixture of biogenic hard and soft components [*Egli*, 2004]. This existence of the two magnetosome components in natural samples has been attributed empirically (using coercivity analysis of remanence curves and transmission electron microscopy) to particle morphology, with elongated grains exhibiting higher coercivities [e.g., *Yamazaki and Ikehara*, 2012; *Lascu and Plank*, 2013]. *Heslop et al.* [2014] have explored the influence of additional factors on the shape of coercivity distributions extracted from FORC central ridges. They concluded that chain length and chain preservation, together with particle morphology and oxidation state, could also explain the occurrence of distinct biogenic coercivity components. Our simulations yield complementary evidence to experimental results [e.g., *Chen et al.*, 2007; *Li et al.*, 2012], and make it increasingly clear that chain collapse may play an important role in determining the shape of coercivity distributions of magnetosome-rich samples.

Hysteresis ratios for chains and isolated particles do not overlap in the Day plot, even for collapsed chains for which $c = 1$ (Figure 3). Fully collapsed chains have high M_{rs}/M_s values ($\sim$0.4) compared to clusters of

strongly interacting particles (~0.2). This might appear at first to be an artifact of the algorithm used to generate chain structures. However, experiments on cultured magnetotactic bacteria show that chains within freeze-dried bacterial cells, which are expected to collapse during the freeze-drying process, have M_{rs}/M_s values in the interval 0.4–0.5, whereas only extracted magnetosomes, which are expected to behave as randomly packed particles, have hysteresis ratios comparable with those of strongly interacting isolated particles [*Moskowitz et al.*, 1993; *Chen et al.*, 2007]. This implies that the physical mechanism of chain collapse preserves vestiges of the chain structure even in fully collapsed chains.

As well as the decrease in overall coercivity and M_{rs}/M_s, our simulations predict very distinctive changes to the FORC diagrams in partially collapsed chains. The results presented in Figure 7 agree very well with experimental FORC diagrams obtained for chains in various degrees of collapse [*Chen et al.*, 2007; *Egli et al.*, 2010; *Kind et al.*, 2011; *Li et al.*, 2012]. A particularly good match is obtained, for example, between Figure 7d for fully collapsed chains (c =1) and *Chen et al.* [2007, Figure 3] for a sample of clustered magnetosomes. Figure 10b shows an example of a FORC diagram obtained on a bulk sediment sample from Brownie Lake, Minnesota that contains a mixture of PSD magnetite and magnetosome chains in various states of collapse [*Lascu et al.*, 2010]. The combination of a sharp ridge signal superimposed on a smooth vertically spread background is very different from that obtained for randomly packed clusters. Such geometry-specific FORC signatures lend credence to the use of FORC diagrams as a diagnostic tool in rock magnetic studies. A new insight from these simulations is that the combination of a sharp ridge and smooth background can be created by homogeneous dispersion of partially collapsed chains, with the relative intensity of the two features a systematic function of the degree of chain collapse. This differs from the traditional interpretation of such signatures in terms of a bimodal mixture of perfectly straight chains and random clusters [*Chen et al.*, 2007; *Kind et al.*, 2011]. The ability to make such distinctions is critical to the interpretation of environmental magnetic signals.

Although the chain configurations explored in Figure 8 are not immediately relevant to magnetotactic bacteria, they serve as a general example of systems with a magnetizing geometry (i.e., those that that create a positive mean-field interaction). The predicted features of the FORC diagram can be observed in many experimental FORC diagrams, suggesting that such geometries are fairly common in nature. An example is shown in Figure 10c. The FORC diagram was obtained for an olivine sample with dislocations that have been decorated with magnetite during heating to 700°C. The area below the horizontal axis contains some of the same features observed for example in Figure 8d: a tilted central ridge with a positive slope and a peak that is offset a few mT to negative B_u, a pronounced negative region, and hints of the boomerang shape above it. The main difference is the absence of signal above the B_c axis in the simulation, indicating that other components are contributing to the signal in the experimental FORC. The examination of simulated FORCs in concert with experimental data could provide insight into the spatial arrangement and the geometry of dislocations in deformed olivine, and whether magnetite particles along dislocations are arranged in clusters or chains with various degrees of separation between particles.

6. Conclusions

One of the primary goals of rock and environmental magnetism is to provide a quantitative characterization of a sample's magnetic mineralogy, with the ultimate aim of producing appropriate physical models. FORC diagrams play an increasingly important role in achieving this goal, due to their sensitivity to magnetostatic interactions between particles. In this paper, we have developed a method for performing routine FORC simulations for arbitrary ensembles of strongly interacting SD particles, and explored some common geometries of relevance to rock and environmental magnetism. Distinctive geometry-specific FORC signatures are obtained, which provide a potential route to extracting a quantitative physical parameterization of the particle ensemble based on the experimental FORC diagram. FORC diagrams of strongly interacting clusters of SD particles share many of the characteristics of FORC diagrams for noninteracting PSD particles, suggesting that the two cases may be closely analogous. Distinctive FORC diagrams for partially collapsed chains of particles provide a new interpretation of experimental FORC diagrams of magnetotactic bacteria in terms of a homogeneous ensemble of chains with a specific degree of chain collapse, rather than a bimodal distribution of straight chains and random clusters. FORC simulations are a valuable tool for the interpretation of experimental FORC diagrams, and should become a routine part of rock magnetic studies.

FORCulator is currently restricted to SD particles. Future work will focus on incorporating simulations for the full range of magnetic behavior (including SP, SD, PSD, and MD states).

References

Bazylinski, D. A., and R. B. Frankel (2004), Magnetosome formation in prokaryotes, *Nat. Rev. Microbiol.*, *2*(3), 217–230, doi:10.1038/nrmicro842.

Carvallo, C., A. R. Muxworthy, D. J. Dunlop and W. Williams (2003), Micromagnetic modeling of first-order reversal curve (FORC) diagrams for single-domain and pseudo-single-domain magnetite, *Earth Planet. Sci. Lett.*, *213*(3-4), 375–390, doi:10.1016/S0012-821X(03)00320-0.

Carvallo, C., A. P. Roberts, R. Leonhardt, C. Laj, C. Kissel, M. Perrin, and P. Camps (2006), Increasing the efficiency of paleointensity analyses by selection of samples using first-order reversal curve diagrams, *J. Geophys. Res.*, *111*, B12103, doi:10.1029/2005JB004126.

Chen, A. P., R. Egli and B. M. Moskowitz (2007), First-order reversal curve (FORC) diagrams of natural and cultured biogenic magnetic particles, *J. Geophys. Res.*, *112*, B08S90, doi:10.1029/2006JB004575.

Dobrotă, C.-I., and A. Stancu (2013), What does a first-order reversal curve diagram really mean? A study case: Array of ferromagnetic nanowires, *J. Appl. Phys.*, *113*(4), 043928, doi:10.1063/1.4789613.

Dunlop, D. J. (2002a), Theory and application of the Day plot (M_{rs}/M_s versus H_{cr}/H_c): 1. Theoretical curves and tests using titanomagnetite data, *J. Geophys. Res.*, *107*(B3), 2056, doi:10.1029/2001JB000486.

Dunlop, D. J. (2002b), Theory and application of the Day plot (M_{rs}/M_s versus H_{cr}/H_c): 2. Application to data for rocks, sediments, and soils, *J. Geophys. Res.*, *107*(B3), 2057, doi:10.1029/2001JB000487.

Egli, R. (2004), Characterization of individual rock magnetic components by analysis of remanence curves, 1. Unmixing natural sediments, *Stud. Geophys. Geod.*, *48*, 391–446.

Egli, R. (2006), Theoretical aspects of dipolar interactions and their appearance in first-order reversal curves of thermally activated single-domain particles, *J. Geophys. Res.*, *111*, B12S17, doi:10.1029/2006JB004567.

Egli, R. (2013), VARIFORC: An optimized protocol for calculating non-regular first-order reversal curve (FORC) diagrams, *Global Planet. Change*, *110*, 302–320, doi:10.1016/j.gloplacha.2013.08.003.

Egli, R., A. P. Chen, M. Winklhofer, K. P. Kodama, and C.-S. Horng (2010), Detection of noninteracting single domain particles using first-order reversal curve diagrams, *Geochem. Geophys. Geosyst.*, *11*, Q01Z11, doi:10.1029/2009GC002916.

Evans, M. E., D. Krása, W. Williams, and M. Winklhofer (2006), Magnetostatic interactions in a natural magnetite-ulvöspinel system, *J. Geophys. Res.*, *111*, B12S16, doi:10.1029/2006JB004454.

Faivre, D., and D. Schüler (2008), Magnetotactic bacteria and magnetosomes, *Chem. Rev.*, *108*(11), 4875–4898, doi:10.1021/cr078258w.

Feinberg, J. M., R. J. Harrison, T. Kasama, R. E. Dunin-Borkowski, G. R. Scott, and P. R. Renne (2006), Effects of internal mineral structures on the magnetic remanence of silicate-hosted titanomagnetite inclusions: An electron holography study, *J. Geophys. Res.*, *111*, B12S15, doi:10.1029/2006JB004498.

Fidler, J., and T. Schrefl (2000), TOPICAL REVIEW: Micromagnetic modelling-the current state of the art, *J. Phys. D. Appl. Phys.*, *33*(15), R135–R156.

Galindo-Gonzalez, C., J. M. Feinberg, T. Kasama, L. C. Gontard, M. Posfai, I. Kosa, J. D. G. Duran, J. E. Gil, R. J. Harrison, and R. E. Dunin-Borkowski (2009), Magnetic and microscopic characterization of magnetite nanoparticles adhered to clay surfaces, *Am. Mineral.*, *94*(8-9), 1120–1129, doi:10.2138/am.2009.3167.

Harrison, R. J., and J. M. Feinberg (2008), FORCinel: An improved algorithm for calculating first-order reversal curve distributions using locally weighted regression smoothing, *Geochem. Geophys. Geosyst.*, *9*, Q05016, doi:10.1029/2008GC001987.

Harrison, R. J., R. E. Dunin-Borkowski, and A. Putnis (2002), Direct imaging of nanoscale magnetic interactions in minerals, *Proc. Natl. Acad. Sci. U. S. A.*, *99*(26), 16,556–16,561, doi:10.1073/pnas.262514499.

Harrison, R. J., R. E. Dunin-Borkowski, J. M. Feinberg, T. Kasama, and E. Simpson (2007), Magnetic properties of rocks and minerals, in *Treatise on Geophysics*, vol. 2, pp. 579–630, Elsevier, Amsterdam, Netherlands.

Heslop, D., A. P. Roberts, and L. Chang (2014), Characterizing magnetofossils from first-order reversal curve (FORC) central ridge signatures, *Geochem. Geophys. Geosyst.*, *15*, 2170–2179, doi:10.1002/2014GC005291.

Kimura, Y., T. Sato, N. Nakamura, J. Nozawa, T. Nakamura, K. Tsukamoto, and K. Yamamoto (2013), Vortex magnetic structure in framboidal magnetite reveals existence of water droplets in an ancient asteroid, *Nat. Commun.*, *4*, 2649, doi:10.1038/ncomms3649.

Kind, J., A. U. Gehring, M. Winklhofer, and A. M. Hirt (2011), Combined use of magnetometry and spectroscopy for identifying magnetofossils in sediments, *Geochem. Geophys. Geosyst.*, *12*, Q08008, doi:10.1029/2011GC003633.

Lappe, S.-C. L. L., N. S. Church, T. Kasama, A. B. da Silva Fanta, G. Bromiley, R. E. Dunin-Borkowski, J. M. Feinberg, S. Russell, and R. J. Harrison (2011), Mineral magnetism of dusty olivine: A credible recorder of pre-accretionary remanence, *Geochem. Geophys. Geosyst.*, *12*, Q12Z35, doi:10.1029/2011GC003811.

Lappe, S.-C. L. L., J. M. Feinberg, A. Muxworthy, and R. J. Harrison (2013), Comparison and calibration of nonheating paleointensity methods: A case study using dusty olivine, *Geochem. Geophys. Geosyst.*, *14*, 2143–2158, doi:10.1002/ggge.20141.

Lascu, I., and C. Plank (2013), A new dimension to sediment magnetism: Charting the spatial variability of magnetic properties across lake basins, *Global Planet. Change*, *110*, 340–349, doi:10.1016/j.gloplacha.2013.03.013.

Lascu, I., S. K. Banerjee, and T. S. Berquó (2010), Quantifying the concentration of ferrimagnetic particles in sediments using rock magnetic methods, *Geochem. Geophys. Geosyst.*, *11*, Q08Z19, doi:10.1029/2010GC003182.

Li, J., W. Wu, Q. Liu, and Y. Pan (2012), Magnetic anisotropy, magnetostatic interactions and identification of magnetofossils, *Geochem. Geophys. Geosyst.*, *13*, Q10Z51, doi:10.1029/2012GC004384.

Li, J., K. Ge, Y. Pan, W. Williams, Q. Liu, and H. Qin (2013), A strong angular dependence of magnetic properties of magnetosome chains: Implications for rock magnetism and paleomagnetism, *Geochem. Geophys. Geosyst.*, *14*, 3887–3907, doi:10.1002/ggge.20228.

Ludwig, P., R. Egli, S. Bishop, V. Chernenko, T. Frederichs, G. Rugel, S. Merchel, and M. J. Orgeira (2013), Characterization of primary and secondary magnetite in marine sediment by combining chemical and magnetic unmixing techniques, *Global Planet. Change*, *110*, 321–339, doi:10.1016/j.gloplacha.2013.08.018.

Ma, C., G. R. Rossman, and J. A. Miller (2007), The origin of color in "Fire" obsidian, *Can. Mineral.*, *45*(3), 551–557, doi:10.2113/gscanmin.45.3.551.

Miot, J., J. Li, K. Benzerara, M. T. Sougrati, G. Ona-Nguema, S. Bernard, J.-C. Jumas, and F. Guyot (2014), Formation of single domain magnetite by green rust oxidation promoted by microbial anaerobic nitrate-dependent iron oxidation, *Geochim. Cosmochim. Acta*, *139*, 327–343, doi:10.1016/j.gca.2014.04.047.

Moskowitz, B. M., R. B. Frankel, and D. A. Bazylinski (1993), Rock magnetic criteria for the detection of biogenic magnetite, *Earth Planet. Sci. Lett.*, *120*, 283–300.

Muxworthy, A. (2003), Effect of magnetostatic interactions on the hysteresis parameters of single-domain and pseudo-single-domain grains, *J. Geophys. Res.*, *108*(B11), 2517, doi:10.1029/2003JB002588.

Muxworthy, A., and W. Williams (2005), Magnetostatic interaction fields in first-order-reversal-curve diagrams, *J. Appl. Phys.*, *97*(6), 63905.

Muxworthy, A., D. Heslop, and W. Williams (2004), Influence of magnetostatic interactions on first-order-reversal-curve (FORC) diagrams: A micromagnetic approach, *Geophys. J. Int.*, *158*(3), 888–897, doi:10.1111/j.1365-246X.2004.02358.x.

Muxworthy, A. R., and D. Heslop (2011), A Preisach method for estimating absolute paleofield intensity under the constraint of using only isothermal measurements: 1. Theoretical framework, *J. Geophys. Res.*, *116*, B04102, doi:10.1029/2010JB007843.

Muxworthy, A. R., D. Heslop, G. A. Paterson, and D. Michalk (2011), A Preisach method for estimating absolute paleofield intensity under the constraint of using only isothermal measurements: 2. Experimental testing, *J. Geophys. Res.*, *116*, B04103, doi:10.1029/2010JB007844.

Newell, A. J. (2005), A high-precision model of first-order reversal curve (FORC) functions for single-domain ferromagnets with uniaxial anisotropy, *Geochem. Geophys. Geosyst.*, *6*, Q05010, doi:10.1029/2004GC000877.

Pike, C., C. Ross, R. Scalettar, and G. Zimanyi (2005), First-order reversal curve diagram analysis of a perpendicular nickel nanopillar array, *Phys. Rev. B*, *71*(13), 134407, doi:10.1103/PhysRevB.71.134407.

Pike, C. R., A. P. Roberts, and K. L. Verosub (1999), Characterizing interactions in fine magnetic particle systems using first order reversal curves, *J. Appl. Phys.*, *85*(9), 6660–6667.

Preisach, F. (1935), Über die magnetische Nachwirkung, *Z. Phys.*, *94*(5-6), 277–302, doi:10.1007/BF01349418.

Roberts, A., L. Chang, D. Heslop, F. Florindo, and J. Larrasoaña (2012), Searching for single domain magnetite in the ''pseudo-single-domain'' sedimentary haystack: Implications of biogenic magnetite preservation for sediment magnetism and relative paleointensity determinations, *J. Geophys. Res.*, *117*, B08104, doi:10.1029/2012JB009412.

Roberts, A. P., C. R. Pike, and K. L. Verosub (2000), First order reversal curve diagrams: A new tool for characterising the magnetic properties of natural samples, *J. Geophys. Res.*, *105*(B12), 28,461–28,475.

Roberts, A. P., F. Florindo, L. Chang, D. Heslop, L. Jovane, and J. C. Larrasoaña (2013), Magnetic properties of pelagic marine carbonates, *Earth Sci. Rev.*, *127*, 111–139, doi:10.1016/j.earscirev.2013.09.009.

Roberts, A. P., D. Heslop, X. Zhao, and C. R. Pike (2014), Understanding fine magnetic particle systems through use of first-order reversal curve (FORC) diagrams, *Rev. Geophys.*, doi:10.1002/2014RG000462, in press.

Schrefl, T., T. Shoji, M. Winklhofer, H. Oezelt, M. Yano, and G. Zimanyi (2012), First order reversal curve studies of permanent magnets, *J. Appl. Phys.*, *111*(7), 07A728, doi:10.1063/1.3678434.

Stancu, A., L. Stoleriu and M. Cerchez (2001), Micromagnetic evaluation of magnetostatic interactions distribution in structured particulate media, *J. Appl. Phys.*, *89*(11), 7260, doi:10.1063/1.1355343.

Stancu, A., C. Pike, L. Stoleriu, P. Postolache, and D. Cimpoesu (2003), Micromagnetic and Preisach analysis of the First Order Reversal Curves (FORC) diagram, *J. Appl. Phys.*, *93*(10), 6620–6622, doi:10.1063/1.1557656.

Stancu, A., L. Stoleriu, P. Postolache, and M. Cerchez (2004), Preisach-type model for strongly interacting ferromagnetic particulate systems, *IEEE Trans. Magn.*, *40*(4), 2113–2115, doi:10.1109/TMAG.2004.830399.

Usov, N. A., and S. E. Peschany (1997), Theoretical hysteresis loops for single-domain particles with cubic anisotropy, *J. Magn. Magn. Mater.*, *174*(3), 247–260, doi:10.1016/S0304-8853(97)00180-7.

Weiss, B. P., E. A. Lima, L. E. Fong, and F. J. Baudenbacher (2007), Paleomagnetic analysis using SQUID microscopy, *J. Geophys. Res.*, *112*, B09105, doi:10.1029/2007JB004940.

Yamazaki, T., and M. Ikehara (2012), Origin of magnetic mineral concentration in the Southern Ocean, *Paleoceanography*, *27*, PA2206, doi:10.1029/2011PA002271.